Diel streamflow cycles suggest more sensitive snowmelt-driven streamflow to climate change than land surface modeling does

Sebastian A. Krogh[1,2,3], Lucia Scaff[4], Gary Sterle[2], James W. Kirchner[5,6], Beatrice Gordon[1], and Adrian Harpold[1,2]

[1]Department of Natural Resources and Environmental Science, University of Nevada, Reno, 89557, USA

[2]Global Water Center, University of Nevada, Reno, 89557, USA

[3]Departamento de Recursos Hídricos, Facultad de Ingeniería Agrícola, Universidad de Concepción, Chillán, 3812120, Chile

[4]Global Water Futures, Canada First Research Excellence Fund (CFREF), University of Saskatchewan, Saskatoon, SK S7N 3H5, Canada.

[5]Department of Environmental Systems Science, ETH Zurich, CH-8092 Zurich, Switzerland

[6]Swiss Federal Research Institute WSL, CH-8903 Birmensdorf, Switzerland

Correspondence to: Sebastian A. Krogh (skrogh@udec.cl)

Abstract. Climate warming will cause mountain snowpacks to melt earlier, reducing summer streamflow and threatening water supplies and ecosystems. Few observations allow separating rain and snowmelt contributions to streamflow, so physically based models are needed for hydrological predictions and analyses. We develop an observational technique for detecting streamflow responses to snowmelt using incoming solar radiation and diel (daily) cycles of streamflow to detect when snowmelt occurs. We measure the date of the 20th percentile of snowmelt days (DOS_{20}), across 31 watersheds affected by snow in the western US, as a proxy for the beginning of snowmelt-initiated streamflow. Historic DOS_{20} varies from mid-January to late May, with warmer sites having earlier and more intermittent snowmelt-mediated streamflow. Mean annual DOS_{20} strongly correlates with the dates of 25% and 50% annual streamflow volume (DOQ_{25} and DOQ_{50}, both $R^2 = 0.85$), suggesting that a one-day earlier DOS_{20} corresponds with a one-day earlier DOQ_{25} and 0.7-day earlier DOQ_{50}. Empirical projections of future DOS_{20} (RCP8.5, late 21st century), using space-for-time substitution, show that DOS_{20} will occur on average 11±4 days earlier per 1°C of warming; however, DOS_{20} in colder watersheds (mean November-February air temperature, $T_{NDJF} < -8$ºC) is on average 70% more sensitive to climate change on average than in warmer watersheds ($T_{NDJF} > 0$ºC). Moreover, empirical space-for-time based projections of DOQ_{25} and DOQ_{50} are about four and two times more sensitive to earlier streamflow than those simulated by NoahMP-WRF under the same scenario. Given the importance of changing streamflow timing for water resources, and the significant discrepancies in projected streamflow sensitivity between space-for-time substitution and a land surface model, snowmelt detection methods such as DOS_{20} based on diel streamflow cycles may constrain models and improve hydrological predictions.

1 Introduction

The role of earlier snowmelt in driving earlier streamflow timing is of great concern in a changing climate (Barnett et al., 2005; Harpold and Brooks, 2018; Musselman et al., 2017; Stewart et al., 2004, 2005). Earlier winter and spring streamflow volume comes at the expense of later summer streamflow in regions like the western US (Hidalgo et al., 2009; McCabe and Clark, 2005; Regonda et al., 2005; Stewart et al., 2004, 2005) and challenges reservoir operations (Barnett et al., 2005; Immerzeel et al., 2020; Viviroli et al., 2011). Furthermore, ecosystems may evaporate more water as reductions in albedo increase energy inputs (Meira Neto et al., 2020), decreasing runoff from upland forested watersheds (Foster et al., 2016; Jepsen et al., 2018; Milly and Dunne, 2020). More than 50% of mountainous watersheds play essential roles in supporting downstream systems (Viviroli et al., 2007) and snowpack changes are likely to increase lowland agriculture water stress (Immerzeel et al., 2020). However, it remains difficult to predict how much streamflow timing and amount will shift in future climates due to altered snow accumulation patterns (Mote et al., 2018), melt rates (Musselman et al., 2017), and shifts from snowfall to rainfall (Klos et al., 2014).

Due to the complexity of upland streamflow generation, physically based hydrological models are typically used to predict how snowpack changes will interact with the critical zone (CZ), and thus affect short-term flood behavior and seasonal water supply forecasts (Kopp et al., 2018; Wood and Lettenmaier, 2006). In mountainous regions like the western US, models need to accurately simulate snow processes across watersheds with varying snowpack conditions (Serreze et al., 1999) and then transport and store that water in the CZ along hillslopes and watersheds with varying subsurface properties (Brooks et al., 2015). More precipitation falling as rain instead of snow will result in streamflow dynamics that more closely mirror the timing of rainfall. Precipitation phase is mediated by basin elevation and hypsometry (Jennings et al., 2018; Wayand et al., 2015), which also influences precipitation amounts (Houze, 2012), with higher elevations and steeper watersheds typically having higher precipitation and snowfall. Solar radiation is the primary energy source for snowmelt in snow-dominated montane watersheds (Cline, 1997; Marks and Dozier, 1992), explaining the importance of cloudiness in regulating snowmelt and streamflow processes, as evidenced by negative correlations between cloud cover and melt rates (Sumargo and Cayan, 2018). Shallower snowpacks have less cold content and begin their melt earlier when solar radiation is lower (Harpold et al., 2012; Harpold and Brooks, 2018; Musselman et al., 2017), which shifts streamflow earlier (Clow, 2010). Storage and drainage of water in the CZ control the sensitivity of streamflow to earlier rain or melt water inputs. For example, snowmelt-mediated spring streamflow timing is more sensitive to climate change in watersheds with rapid subsurface drainage than in landscapes with deep groundwater reservoirs that drain slowly (Safeeq et al., 2013). In contrast, the sensitivity of snowmelt-mediated summer streamflow volume to climate change has shown to be higher in slow-draining watersheds (Tague and Grant, 2009). The complexity of these storage relationships is exemplified by isotopic evidence showing that the fraction of streamflow that

is "young water" (less than three months old) is smaller in steeper watersheds (Jasechko et al., 2016), suggesting that interactions between CZ water storage and changing hydrometeorology will be challenging to predict in mountainous areas.

Hydrologists typically apply two types of modeling tools to predict future streamflow: empirical models (such as space-for-time substitutions) and more mechanistically oriented models (conceptual or physically based land surface models). Space-for-time substitution assumes that long-term site-to-site statistical relationships among variables (e.g., precipitation and air temperature) can be used to understand and model their likely changes over time (e.g., evapotranspiration and streamflow). Space-for-time substitution has been used in fields such as hydrology (Goulden and Bales, 2014; Jepsen et al., 2018; Sivapalan et al., 2011), biodiversity (Blois et al., 2013) and tree growth (Klesse et al., 2020) to predict responses to climate change. A limitation of the space-for-time approach is that it neglects non-correlated (or independent) changes in spatially varying factors (Jepsen et al., 2018). For example, heterogenous patterns of warming, variations in precipitation and vegetation, or changes that occur at different temporal scales (e.g., soil properties versus rain-snow line transition) are implicitly neglected in the space-for-time approach. Conversely, physically based models embed physics and state-of-the-art understanding of hydrological processes. These models typically require some degree of calibration or validation to observations (e.g., daily streamflow) to increase and assess their predictive skill. The current generation of regional weather models using the Weather Research and Forecasting model (WRF) (Skamarock et al., 2008) coupled to the Noah Multi Parameterization land surface model (Noah-MP) (Niu et al., 2011) has shown promising results for modeling atmospheric and snow processes in the contiguous US (He et al., 2019; Liu et al., 2017; Musselman et al., 2017; Scaff et al., 2020). For example, snow simulations have been used to quantify mountain snowmelt and streamflow response to climate change (Musselman et al., 2017, 2018). These simulations use a pseudo global warming approach, which perturbs the historical climate with a climate change signal from an ensemble of global climate models (GCMs); using this perturbation avoids systemic biases in the GCMs and avoids issues related to their interannual variability (Liu et al., 2017). Given the importance of snowmelt to streamflow generation and its uncertain sensitivity to climate change, new tools that allow comparisons between land surface models and space-for-time predictions of future streamflow are valuable, and could help to diagnose modeling issues that can be improved for better predictions.

Few simple, low-cost observational tools exist to separate rainfall-driven from snowmelt-driven contributions to streamflow or to separate this year's melt from previous years' melt and storage. One method that can be straightforwardly applied to existing long-term observations is based on coupled diel cycles in solar radiation, snowmelt, and streamflow (Kirchner et al., 2020; Lundquist and Cayan, 2002). Diel (24-hours) cycles in streamflow and shallow groundwater levels are often found in mountainous systems driven by either snow or ice melt and evapotranspiration, which are both ultimately driven by solar radiation inputs (Kirchner et al., 2020). This mechanistic response has been used to study watershed properties like kinematic wave celerity (Kirchner et al., 2020), the impact of snowpack variability on streamflow timing (Lundquist and Dettinger, 2005), groundwater fluctuations (Loheide and Lundquist, 2009), and transitions from snowmelt to evapotranspiration-

dominated streamflow fluctuations (Kirchner et al., 2020; Mutzner et al., 2015; Woelber et al., 2018). More recently, Kirchner et al. (2020) combined local observations and remote sensing to show that streamflow diel response was tightly controlled by the timing of snowpack disappearance. Here, we extend the 'diel cycle index' approach of Kirchner et al. (2020) using diel streamflow observations to detect the occurrence of days when streamflow is coupled to snowmelt inputs, and investigate their contributions to historical variability in streamflow amount and timing. We compare space-for-time end-of-century predictions under an RCP8.5 pseudo global warming scenario against predictions from a state-of-the-art land surface model (under the same climate scenario) across 31 mountainous watersheds in the western US to answer the following questions:

1. Is there evidence of earlier snowmelt in warmer watersheds and years, and can we use the timing of snowmelt to predict the timing of streamflow volume?
2. How does snowmelt timing predict streamflow volume timing with a space-for-time approach and where is the timing of snowmelt most sensitive to climate change?
3. Do historical streamflow volume timings and future space-for-time-based projections diverge from commonly used, state-of-the-art land surface models?

A list with the abbreviations used in this study is presented in Table 1.

2 Methods

2.1 Study Domain and Data

We studied snowmelt-driven streamflow in 31 mountainous watersheds in the western US (Table 2), spanning snow fractions of 0.27 to 0.78 (Figure A3A), aridity index values from 0.22 to 2.86 (Addor et al., 2017), and soil depths from 0.27 to 2.52 m (Addor et al., 2017; Pelletier et al., 2016) (Table 2). These watersheds are part of the CAMELS (Catchments Attributes and MEteorology for Large-sample Studies) dataset (Addor et al., 2017; Newman et al., 2015), which provides daily streamflow and meteorological forcing, among other observed and simulated hydrometeorological variables at the watershed scale. These watersheds were chosen because their streamflows are unregulated, they have relatively small drainage areas (< 250 km^2), and they are at relatively high elevations (> 1,000 masl). This last criterion was introduced to focus on watersheds with snowmelt-driven streamflow regimes. The names, locations, elevations, slopes, drainage areas and other key characteristics of the 31 watersheds are presented in Table 2.

The data used in this analysis include hourly streamflow and incoming shortwave radiation, and mean daily relative humidity, air temperature and precipitation. Hourly streamflow was obtained from the US Geological Survey. Hourly incoming shortwave radiation is from phase 2 of the National Land Data Assimilation System (NLDAS-2) (Xia et al., 2012) at the nearest grid point to the watershed outlet. Mean daily relative humidity, air temperature and precipitation at the watershed scale are from CAMELS, based on the DAYMET dataset (daymet.ornl.gov), which in turn is interpolated from existing ground observations. Available hourly streamflow records vary significantly across watersheds, extending back to 1986 for some sites. Figure A1A shows the number of years that have more than 70, 80 and 90% of days with hourly records for the period between

December 1 and August 1. Based on this preliminary analysis, we decided to use water years with more than 80% of days with hourly streamflow records. This threshold for data availability results in most watersheds having more than 5 years to analyze (except for sites #10 and #30 with 4 years).

2.2 Snowmelt and Streamflow Diel Coupling

To infer the occurrence of days when solar radiation-driven snowmelt is coupled to the streamflow, hereafter referred as snowmelt days for simplicity, we calculated the correlation between hourly values of solar radiation and lagged streamflow (Figure 1). A snowmelt day is defined as a day in which the Spearman correlation between hourly solar radiation and lagged streamflow is statistically significant (p-value$\leq$0.01) and exceeds a given cutoff. Due to the lagged diel streamflow response after snowmelt, we lagged diel streamflow from solar radiation between 6 and 18 hours, computed the correlation of all combinations, and kept those statistically significant correlations that were above a pre-defined correlation cutoff. Although having both a correlation cutoff and a statistical significance criterion may be redundant, we used both to guarantee significant correlations above different correlation cutoffs. We tried several correlation cutoffs ($r>0.5$, 0.6, 0.7, 0.8 and 0.9; see Figure 1 for $r>0.6$) to assess their effects on the detection algorithm (Figure A2). The preliminary lag window of 6 to 18 hours was used to avoid confounding snowmelt signals with evapotranspiration (ET)-induced streamflow diel responses (Kirchner et al., 2020; Mutzner et al., 2015; Woelber et al., 2018). ET-induced streamflow diel response can positively correlate with solar radiation with lags below 6 hours due to the previous day's ET, and above 18 hours due to the next day's ET diurnal signal (Kirchner et al., 2020). However, this preliminary lag window may incorrectly select days with a rainfall-induced streamflow diel response or rain-on-snow events. To minimize this, we further restricted the lags that could be selected based on optimum lags from snowmelt days with clear skies. Clear-sky days were defined as days with solar radiation greater than 80% of the clear-sky solar radiation (grey areas in left panels on Figure 1). This lag window was defined on a monthly and watershed basis and was calculated as the lags between the 10^{th} and 90^{th} percentile of clear-sky days with Spearman correlations above 0.8. This second filter also helped to avoid the incorrect selection of ET-induced streamflow diel response, as it minimized the chance of selecting 18-hr lags that can be associated with ET. Despite efforts to select only snowmelt-driven streamflow diel responses, this methodology does not guarantee that rainfall-driven streamflow diel changes with lags within our lag window will always be excluded. Excluding such cases would require hourly precipitation observations, which are not available for all of our study watersheds. However, we believe that any such cases will minimally affect the results of our analysis.

To provide a better idea of the potential impact that rainfall may have on our proposed diel analysis, particularly on the effect of rain-on-snow events, we analyzed which days that were classified as snowmelt days also has rainfall. We assessed daily rainfall using the daily precipitation time series from CAMELS based on the DAYMET product for each watershed. A false detection rate metric was computed for each watershed, in which every day classified as a snowmelt with daily precipitation above 5 mm and a mean daily air temperature above 2 ^{o}C was assumed to be mis-classified (Figure 2). A false detection rate of 100% means that all snowmelt days were mis-classified and 0% means that no days had significant rainfall. On average,

the false detection rate was estimated at 7% with a standard deviation of 5%, and only watersheds #24 and #31 (located in WA and OR, respectively) are above 15%, with 21% and 29%, respectively. This suggest that the effect of potential rainfall-induced diel streamflow cycle (including rain-on-snow events) in most watersheds is low (except for watersheds #24 and #31), supporting further analysis. We also assessed the mean cross-site false detection rate for precipitation thresholds of 1 mm and 10 mm and found reasonable values of 12% and 3%, respectively. However, we believe that 1 mm is not a reasonable threshold as a 1 mm rainfall event is unlikely to produce a distinguishable diel streamflow signal or could represent error/noise in the DAYMET product.

2.3 Space-for-Time substitution for DOS_{20}

We defined the day when the 20th percentile of the snowmelt days occurs (DOS_{20}) as a new metric to characterize the seasonality of early snowmelt for each water year and watershed. However, other metrics such as the 5th, 10th and 30th percentiles (presented in the appendices) were also investigated to assess the impact of this choice on the analysis. We chose this metric because we expect it to be associated with the timing of streamflow volume, and the choice of slightly earlier or later snowmelt days would not substantially change our results. We fitted a stepwise multiple linear regression model (MLR, p-value<0.01, Equation 1) to reconstruct historical DOS_{20} across all our sites (Figure A4) using four climate variables: total precipitation, air temperature, relative humidity, and solar radiation.

$$DOS_{20} = \beta_1 x_1 + \beta_2 x_2 + \beta_3 x_3 + \beta_4 x_4 + \beta_5 x_1 x_2 + \beta_6 x_1 x_3 + \beta_7 x_1 x_4 + \beta_8 x_2 x_3 + \beta_9 x_2 x_4 + \beta_{10} x_3 x_4 \quad (1)$$

Where x_1 is cumulative air temperature (°C), x_2 is cumulative precipitation (mm), x_3 is mean relative humidity (%), x_4 is mean solar radiation (W m^{-2}), and β_i are the regression coefficients. Mean annual climate variables were calculated for the period between November 1st and DOS_{20}. This results in DOS_{20} being present in both sides of Equation 1; therefore, the stepwise MLR requires an iterative solution when used in a predictive mode (i.e., for the climate change analysis). We verified the stepwise MLR assumptions, namely, linear relationships between each predictor and DOS_{20}, normally distributed residuals, homoscedasticity, and absence of strong multicollinearity (as suggested by a Variance Inflation Factor < 3). We also tested other metrics related to the timing of early snowmelt events. These included: the first snowmelt day, the first three consecutive snowmelt events, and the 5th, 10th and 30th percentiles of snowmelt days (DOS_5, DOS_{10} and DOS_{30}, respectively). All these metrics were also computed using each of the different Spearman correlation cutoffs (Table A1, A2, A3, A4 and A5), but the main analysis presented here focuses on DOS_{20} based on snowmelt days calculated with hourly Spearman correlations >0.8. We used a space-for-time approach to predict changes to DOS_{20} based on the stepwise MLR model and an end-of-the-century mean climate change signal from WRF (Liu et al., 2017). WRF was run under a high emission scenario (RCP8.5) using the pseudo global warming approach for the end of the century. Overall, it projects a warmer (4 – 5.2°C) and wetter (0 - 20% increase in precipitation) climate (Figure A4 and A5). As previously mentioned, predictors used in the stepwise MLR are calculated for the period between November 1st and DOS_{20}; therefore, as we do not know the value of DOS_{20} in the future, an

iterative solution is required to solve for DOS_{20} in Equation 1. We find a numerical solution using a 2-day convergence threshold between iterations, so that $|DOS20_{i+1} - DOS20_i| \leq 2$ days, where '*i*' is the number of the iteration.

2.4 Streamflow Volume Timing from a Land-Surface Model

Historical NoahMP-WRF simulations include the period 2001-2013 over the contiguous US at 4-km spatial resolution, and the period 2071-2100 under pseudo global warming (Liu et al., 2017). NoahMP-WRF simulations include an improved Noah configuration aiming to better represent the snow physics. These improvements include (Liu et al., 2017): the rain-snow transition is based on a microphysics partitioning approach as opposed to a subjective temperature-based approach, patchy snowpack are allowed in the calculation of the surface energy balance, the heat transport from rainfall to the ground is included, and the snow depletion curve is vegetation-dependent. These improvements allow a better representation of the surface energy balance, and the simulation of snow accumulation and melt processes. We used daily watershed-scale outputs of surface and subsurface runoff from historical and future NoahMP-WRF simulations to estimate DOQ_{25} and DOQ_{50}. Given the range of the watershed drainage areas (4 - 236 km^2, Table 2), watersheds covering several grid cells use the total surface and subsurface runoff for their corresponding grid cells. Small watersheds are represented by only the single nearest NoahMP-WRF grid cell. The way NoahMP-WRF is implemented within WRF lacks a streamflow routing scheme such as the one in WRF-Hydro (Gochis et al., 2020); therefore, we use the sum of surface and subsurface runoff to estimate DOQ_{25} and DOQ_{50}. We also repeated the analysis using surface runoff only, leading to similar results (Figure A7). Given the relatively coarse NoahMP-WRF spatial resolution (4 km) compared to the watershed drainage areas (4 - 236 km^2), we expect that mean streamflow timing metrics will not be significantly affected by the lack of streamflow routing.

3 Results

3.1 Empirical Relationships Between DOS_{20}, Climate and Streamflow

Mean DOS_{20} has a strong regional variability that is reasonably captured by a negative linear correlation ($R^2 = 0.48$) with the mean winter air temperature (November to February, T_{NDJF}) in watersheds with T_{NDJF}<-3°C, whereas warmer watersheds do not follow the same pattern (Figure 3A and Figure 4A). Warmer sites (T_{NDJF} > -3 °C) have a more variable mean DOS_{20} ranging from mid-January to early May, whereas the coldest sites (T_{NDJF} <-8°C) have a later and less variable DOS_{20} around mid to late May. On average, the regression suggests that a 1 °C of warming results in 7.2-day earlier DOS_{20}. The relationship between later DOS_{20} and colder T_{NDJF} is also found in the year-to-year variations in DOS_{20} at most watersheds (21 out of the 31), with warmer years experiencing earlier DOS_{20} (Figure 3B). A strong linear relationship was found between the date of the 25% of the annual streamflow volume (DOQ_{25}) and T_{NDJF}. Warmer watersheds (T_{NDJF}>0°C) generate streamflow the earliest (between mid-December and early March) compared to the coldest watersheds (T_{NDJF}<-8°C), with DOQ_{25} between early and late May (Figure 3C). On average, the cross-site regression shows that a 1°C increase in T_{NDJF} produces a 13-day earlier DOQ_{25}. For most watersheds (25 out of 31), interannual regressions show a similar pattern with warmer years having earlier DOQ_{25};

however, these interannual regressions have shallower slopes than the cross-site relationship (Figure 3B and 3D). Previous work by Stewart et al. (2005) also related seasonal meteorological patterns with the spring onset and streamflow timing, and found similar relationships (e.g., warmer watersheds have earlier spring onset and streamflow timing). However, the definition of the spring onset was based on the cumulative hydrograph (the day when the cumulative departure from the mean streamflow was the minimum), as opposed to our more mechanistic diel streamflow analysis. Other definitions for spring onset based on streamflow, snow pillows and air temperature are presented by Lundquist et al. (2004).

Strong correlations between DOS_{20} and both DOQ_{25} and DOQ_{50} (the dates at which 25% and 50% of the annual streamflow volume are reached) (R^2 = 0.85, Figure 5A and 5C) suggest connections between the timing of snowmelt and streamflow generation across watersheds and years. On average, sites that melt earlier are associated with earlier DOQ_{25} (Figure 5A) and a lower ratio of snowfall to total precipitation (snow fraction<0.5). The relationship between DOS_{20} and DOQ_{25} closely follows the 1:1 line (Figure 5A), although three sites in Washington and Oregon (sites #24, #25 and #31, see Table 2 and Figure 6A) deviate substantially from this pattern, perhaps because they receive relatively little of their precipitation as snow. Similar watershed-level relationships using interannual variability in DOQ_{25} were found for most watersheds, with statistically significant slopes varying between 0.4 and 2.5 day day^{-1} (Figure 5B). DOS_{20} also predicts DOQ_{50} well, with 10-day earlier snowmelt producing 7-day earlier DOQ_{50} on average (Figure 5C), and similar watershed-level interannual relationships (Figure 5D). The same three relatively rainy watersheds have DOQ_{50} prior to the DOS_{20} (Figure 5C and Figure 6B), suggesting that early snowmelt timing is not an important predictor of DOQ_{50} in such places.

3.2 Sensitivity of Snowmelt Timing (DOS_{20}) to Climate Change: Space-For-Time Substitution

We fitted a stepwise MLR with four climate variables (air temperature, precipitation, relative humidity, and solar radiation) to predict DOS_{20} across watersheds and years. A total of 333 watershed-year combinations of DOS_{20} and climate variables were used to train the stepwise MLR model. The watershed-year relationship between observed and MLR predictions has a relatively high R^2 of 0.83, a root mean square error (RMSE) of 17.5 days, and normally distributed residuals ($p < 0.01$) off the 1:1 line and centered at 0 with a standard deviation of 17.3 days (Figure 7A). The relationship between observations and MLR predictions of inter-watershed mean annual DOS_{20} (Figure 7B) is also strong (R^2 = 0.83 and RMSE = 13.2 days) and follows the 1:1 line. Similarly, when we look at interannual values, represented by the lines overlapping circles in Figure 7B, we find a good agreement, with most slopes are close to 1:1 (see inset plot Figure 7B). This analysis demonstrates that the MLR model can reasonably represent both the mean annual DOS_{20} values at each watershed and their interannual variability. Table A4 shows standardized beta coefficients that indicate the importance of each climate variable in the stepwise MLR. For the 0.8 correlation cutoff we found that incoming shortwave radiation has the greatest importance (beta = 0.75), followed by relative humidity (beta = 0.37) and air temperature (beta = -0.31).

Space-for-time projections under climate change show earlier mean annual DOS_{20} in all watersheds, with significant variability from site to site (Figure 8A). Most watersheds show significant end-of-century changes in DOS_{20} ranging from up to three months earlier in cold sites where, historically, snowmelt under clear-sky conditions dominates (circles in Figure 8A), to as little as 20 days earlier in warm sites under historically cloudier conditions. The cross-site average change in DOS_{20} is 55.3 days with a standard deviation of 21.8 days. In many watersheds the mean projection of DOS_{20} under climate change is within the historically observed variability in DOS_{20} (Figure 8A). Space-for-time substitution predicts that colder watersheds ($T_{NDJF} \leq$ -8°C) on average are about 70% more sensitive to climate change (13.7±4.6 days $^{\circ}C^{-1}$) than warmer watersheds are (T_{NDJF}>0°C) (8.1±6.2 day $^{\circ}C^{-1}$), as represented by the change in the DOS_{20} per degree of warming (Figure 8B). Site #24 (South Fork Tolt River, WA.) shows almost no change in its DOS_{20}, which can be attributed to its weaker climate change signal compared to the other watersheds (about +4°C, 5% precipitation increase, and virtually no change in humidity and solar radiation; Figure A4). When we look at the mean sensitivity across all watersheds, the space-for-time analysis suggest an average sensitivity of 11.1±4.2 days $^{o}C^{-1}$.

3.3 Sensitivity of Streamflow Timing to Climate Change: Space-for-time versus NoahMP-WRF

We compared historical and space-for-time projections for DOQ_{25} and DOQ_{50} with those from NoahMP-WRF. Streamflow sensitivity using space-for-time projections for DOS_{20} under climate change were built using the linear regressions presented in Figure 5A and 5C (DOQ_{25} and DOQ_{50} vs DOS_{20}). Space-for-time projections for DOQ_{25} range from early January to late May (red symbols, Figure 9A), advancing between 20 and 100 days under RCP 8.5 (x-axis, Figure 9C). The DOQ_{50} is projected to advance between roughly 15 and 65 days (x-axis, Figure 9D), ranging from mid-February to late May (red symbols, Figure 9B). The historical DOQ_{25} is greatly underestimated by NoahMP-WRF (blue symbols, Figure 9A) with a mean DOQ_{25} in mid-February, whereas historical DOQ_{25} is in early April (50-day mean difference). Projected changes to DOQ_{25} by NoahMP-WRF under pseudo global warming range between early January to mid-March (mean in early February), whereas space-for-time projections range between early January and late March (mean in mid-February; Figure 9A). These results indicate that space-for-time projections of DOQ_{25} are about four times more sensitive to climate change than those from NoahMP-WRF (ΔDOQ_{25} averages about -60 days for space-for-time substitution and -15 days for NoahMP-WRF; Figure 9C). Historical DOQ_{50} is reasonably well represented by NoahMP-WRF under the current climate (blue symbols, Figure 9B) with a mean difference of only 7 days, but future changes of about -20 days are roughly half of the -40 days predicted by the space-for-time projections (Figure 9D). Space-for-time projections of DOQ_{50} range between mid-February and early April, whereas NoahMP-WRF projections range between mid-March and mid-May. Watersheds with the largest disagreement between space-for-time and NoahMP-WRF projections for streamflow volume timing are those where DOS_{20} is the most sensitive to climate change, represented by the orange and yellow symbols in Figure 9C and 9D. These watersheds are characterized by historical cold winter temperatures (T_{NDJF}<-6°C) with snowmelt occurring mostly under sunny conditions (circle symbols) and are mostly located in the Rocky Mountains.

4 Discussion

The new DOS_{20} metric describes the timing of early snowmelt-mediated streamflow based on the diel streamflow fluctuations and suggests that shifts in snowmelt timing in colder, sunnier watersheds have a greater effect on streamflow volume timing than in warmer, cloudier watersheds where snowmelt is more interspersed with rain. Despite the intuitive connections between snowmelt and streamflow, empirically linking changes in earlier snowmelt rates (Harpold and Brooks, 2018; Musselman et al., 2017) with changes in streamflow amount (Barnhart et al., 2016) and timing (Stewart et al., 2004) has been challenging (Weiler et al., 2018), partly due to the scales at which snow (point-scale) and streamflow (watershed-scale) are typically measured. For example, evidence of snowmelt at Snow Telemetry (SNOTEL) locations in the US has shown that snowmelt events are more intermittent at sites with higher humidity, and future modeling suggests slower, earlier snowmelt in the largest snowpacks in areas with lower humidity and cloud cover (Harpold and Brooks, 2018; Musselman et al., 2017). However, the potential cascading effects of earlier and slower snowmelt on streamflow amount and timing are relatively unexplored (e.g. Berghuijs et al., 2014). Not surprisingly, the warmest and cloudiest watersheds have lower snow fractions and a more rainfall-dominated streamflow regime, and thus have less (and often no) interannual correlation between DOS_{20} and the metrics DOQ_{25} and DOQ_{50} (Figure 5A and 5C), illustrating the limitations of the diel streamflow method in rain-dominated watersheds; as also suggested by the false detection rate analysis (Figure 2) in watersheds #24 and #31 in Washington and Oregon, respectively. Rain-on-snow events are particularly challenging to detect with our analysis, as days with low percentage of incoming shortwave radiation (<80% of clear-sky) are filtered out to avoid issues with potential rainfall-dominated diel signals. Conversely, the colder and sunnier watersheds, primarily in the intermountain region, have strong interannual correlations between DOS_{20} and DOQ_{25} (Figure 5A and Figure 6A), reflecting the importance of snowmelt (instead of rain) in controlling streamflow volume timing. We currently lack physically based representations of many processes linking snowpack storage, snowmelt, subsurface storage, and the timing of water release following a hydrologic event (i.e., snowmelt or rainfall event). Snowmelt modeling in complex terrain is challenged by steep climate gradients and by the lack of adequate forcing data required to run models. Characterizing precipitation phase and timing in steep watersheds remains challenging in rain-to-snow transition zones (Harpold et al., 2017; Jennings et al., 2018; Wayand et al., 2015), which will presumably increase in extent in the future (Klos et al., 2014). Complex terrain has a large effect on radiation fluxes, which are hard to capture at kilometer spatial scales (Müller and Scherer, 2005) used in some land surface models. Nonetheless, this issue is less important in warmer, cloudier watersheds where longwave radiation and sensible heat are larger components of the energy balance (Mazurkiewicz et al., 2008). Forests exert a strong control on the snowpack mass and energy balance (Lundquist et al., 2013; Pomeroy et al., 1998; Safa et al., 2021) with spatially heterogeneous effects on snow accumulation and melt that remain challenging to model (Broxton et al., 2015; Krogh et al., 2020). The presence of preferential flowpaths through the snowpack impacts the timing of melt release (Leroux and Pomeroy, 2017) and is not typically included in hydrological models. Once snowmelt is released from the snowpack, simulating (and validating) what fraction flows as subsurface and surface runoff remains difficult. Decades of tracer studies (e.g., Godsey et al., 2010; Kirchner, 2003) have shown that streamflow during and after hydrologic events

(i.e., snowmelt or rainfall events) is typically 'old water' that has been stored in the watershed for months to years. Land surface models like NoahMP-WRF lack realistic groundwater stores to represent old water and are at spatial resolutions that make hillslope and near-stream processes difficult to represent (Fan et al., 2019). For example, previous work at Sagehen Creek (site #23) suggests that streamflow remains ~80% groundwater even during the snowmelt freshet (Urióstegui et al., 2017). Innovative observations and/or analyses that give new physical insights, like the diel streamflow analysis, can be used to derive such hydrologic representations, which could improve our prediction of hydrological systems (Kirchner, 2006).

Because the diel analysis does not require assumptions embedded in physically based models, it is an independent tool that can be used to verify historical streamflow simulations from sub-daily resolved hydrological models. For example, land surface models could be benchmarked against observed snowmelt days based on the diel analysis or metrics like the DOS_{20}, aiming to better represent processes associated with snowmelt-driven streamflow generation. The diel analysis is also easier to implement than detailed process-based catchment models because it only requires observed hourly streamflow data and solar radiation. Solar radiation can be reliably represented by land surface models with data assimilation like NLDAS-2 (Luo et al., 2003) that assimilate field observations and remotely sensed radiation (including the effects of clouds) into an atmospheric modeling framework. We tested the sensitivity of some modeling decisions, such as the correlation cutoff between hourly solar radiation and streamflow used to detect snowmelt days and metrics for snowmelt timing and found similar sensitivities of DOS_{20} to climate change across different correlation cutoffs and snowmelt timing percentiles (Table A5). Metrics like the first snowmelt day or the first three consecutive snowmelt days showed less consistent results (Table A5), likely due to individual early or mid-winter melt events that do not necessarily represent the seasonal watershed behavior. The diel streamflow analysis has four main limitations that need to be examined in future work: (1) it requires a steep enough stage-discharge relationship that daily streamflow cycles can be detected across the flow regime, (2) it focuses on snowmelt driven by solar radiation (and energy fluxes synchronized with it), (3) it is sensitive to assumptions about the lag time between solar radiation and streamflow, and (4) it is sensitive to assumptions about evapotranspiration losses. A steep stage-discharge relationship, in which small changes in discharge are associated with large changes in stage, is ideal to observe small diel streamflow changes with sufficient precision. Another assumption is that the majority of snowmelt is correlated with solar radiation. This assumption is supported by the importance of solar radiation in process-based studies of maritime and continental snowpacks (Cline, 1997; Jepsen et al., 2012; Marks and Dozier, 1992). Because our method allows the lag time between solar radiation and streamflow to vary within a predefined window, we expect it to capture other important energy fluxes like sensible heat that often lag the diel patterns of solar radiation by several hours (Ohmura, 2001). This approach is not suitable for capturing rain-on-snow events, which are most common in maritime watersheds, but also occur in continental settings (Musselman et al., 2018). It may also misclassify rainfall-driven diel streamflow cycles, although we checked for rainfall-induced cycles and found that these are, on average, a small fraction (7%, Figure 2). In rainier watersheds (lower snow fraction), our analysis may be more uncertain than in watersheds with a more snowfall-dominated regime. Nonetheless, the relationships between streamflow timing (i.e., DOS_{20}, DOQ_{25} and DOQ_{50}) and meteorological drivers in rainier sites showed cross-site and interannual

relationships that are consistent with those in colder, more snow-dominated places (except for watersheds #24, #25 and #31) (e.g., Figure 3A and 3C). The third limitation is that the spatiotemporal variability in snowpack, surface and subsurface storage, and evapotranspiration will change the magnitude and lag time of the diel streamflow response (Kirchner et al., 2020; Lundquist and Cayan, 2002; Lundquist and Dettinger, 2005), which we address by allowing variable watershed- and month-specific time lags. However, lag times greater than 24 hours, which are associated with large watersheds or large subsurface storage, will make this method imposible to apply. Also, the method may miss early snowmelt-driven diel cycles in watersheds with dry soils, as the diel signal will be buffered by the subsurface storage capacity before generating a measurable streamflow response. The fourth limitation is that evapotranspiration losses must be small relative to snowmelt inputs, which is necessary because the effect of evapotranspiration is out of phase with the effect of snowmelt (Kirchner et al., 2020). Evapotranspiration effects are minimized by focusing on early snowmelt when evapotranspiration losses are often assumed to be small (Bowling et al., 2018; Cooper et al., 2020; Winchell et al., 2016).

Previous space-for-time implementations have been used to predict catchment-scale sensitivity of snowmelt-driven streamflow to changing climate using observations (Berghuijs et al., 2014; Stewart et al., 2005) and historical model outputs (Barnhart et al., 2016). Our MLR results suggest that humidity explains roughly as much or more variation in DOS_{20} than temperature does (Table A4), and that solar radiation explains about twice as much DOS_{20} variation as either humidity or temperature does. This is consistent with an energy budget dominated by solar radiation (Marks and Dozier, 1992), but also with a coupling between humidity and latent heat and longwave radiation effects (Harpold and Brooks, 2018). Space-for-time projections of DOS_{20} under the pseudo global warming scenario show that colder, drier, and sunnier sites (typical of the Rocky Mountains) are about twice as sensitive to warming as warmer, more humid, and cloudier sites (typical of the Pacific Northwest). Humid and warmer sites have relatively low snow fractions (<0.5, more rainfall effects) and, thus, a smaller snowmelt signal in the diel streamflow observations. In contrast, Harpold and Brooks (2018) showed that winter ablation at SNOTEL sites in humid places, like the Pacific Northwest, are more sensitive to warming than less humid places, like the Southwest US. The difference between these findings and our streamflow-based inferences might be explained by SNOTEL sites being preferentially situated in snowy forest gaps that do not necessarily represent the catchment-scale, early-season snowmelt patterns focused on here. However, Kirchner et al. (2020) show general agreement between SNOTEL snowmelt response and the snowmelt-induced diel streamflow signal at the warm Sagehen Creek watershed (site #23). The sensitivity of the early snowmelt timing metric (DOS_{20}) to climate change may be distilled into streamflow´s sensitivity to changes in precipitation partitioning (rainfall vs snowfall) and snowmelt sensitivity (more energy for melt is available); however, these two are sometimes coupled (e.g., changes in snow albedo after snowfall will alter the energy balance that controls snowmelt). Due to the empirical basis of our analysis, these two sensitivities are not easy to disentangle, but we believe that the diel analysis is better suited to investigate streamflow´s sensitivity to snowmelt changes. We focus the analysis on mostly clear-sky days, and thus implicitly exclude the effect of rainfall (or precipitation partitioning); we also use predictive variables in the MLR that relate to broad and regional snowmelt controls (i.e., seasonal meteorology) as opposed to specific event-scale meteorology required to predict precipitation

partitioning. The reliability of the space-for-time projections partially depends on whether climate projections are within or outside the range of observed climate conditions. Under the pseudo global warming scenario, cold, sunny watersheds like those in the Rocky Mountains (site #9 and #10) will shift toward more humid, warmer conditions (Figure A6), like those observed in Southern Idaho (site #29) and the northern Sierra Nevada (site #23). In contrast, the pseudo global warming scenario in places like the Pacific Northwest, particularly those involving changes in atmospheric humidity above 5 g/m^3 (Figure A4), have not been observed, and therefore are more uncertain. Overall, climate changes from pseudo global warming are mostly within the observed interannual and inter-watershed climate variability used to train the stepwise MLR (Figure A4). Space-for-time substitution assumes that other variables not included in the analysis vary together with the predictive variables (climate), and neglects variables like the catchment's physical (e.g., soil storage) and biological (e.g., vegetation) properties that do not necessarily co-vary with climate. Determining under what conditions we can reasonably apply space-for-time remains an open question and has been posed as one the 23 unsolved problems in hydrology (Blöschl et al., 2019), highlighting the value of comparing our space-for-time approach to a physically-based model.

The sensitivity of historical snowmelt-mediated streamflow volume timing (DOQ_{25} and DOQ_{50}) to climate change differs between the space-for-time approach and a land surface model, particularly in cold watersheds (Figure 9C and 9D), raising questions about current state-of-the-art projections of early season streamflow timing from NoahMP-WRF. The observed data used in the space-for-time approach have larger and more variable streamflow timing responses to climate change (10 – 17 days $°C^{-1}$) in cold, drier, sunnier places that are representative of small, high-elevation Rocky Mountain watersheds (Figure 8B). The historical diel streamflow analysis suggests that NoahMP-WRF may be systematically under-predicting the sensitivity of streamflow volume timing to earlier snowmelt-induced streamflow in colder and sunnier places (Figure 9C) that are most likely to have increased temperature and increased cloudiness in the future. The same mean annual future climate scenarios were applied to both approaches; however, important differences in the streamflow timing response were found between NoahMP-WRF and the space-for-time projections (Figure 9C and 9D). NoahMP-WRF underpredicts DOQ_{25} (Figure 9A) across most sites, whereas the DOQ_{50} is much better represented. Historically, NoahMP-WRF performed the best in rainier sites (see circled blue symbols in Figure 9A) and other sites classified as 'cloudy' and 'partly cloudy', whereas the Rocky Mountain sites, characterized by 'sunny' snowmelt event, were among the most biased (see blue filled circles in Figure 9A). This suggest that the timing of streamflow volume is better represented in areas where snowmelt processes are less important, though other variables like topographic and climatic gradients can also be important. It is worth noting that when DOQ_{25} simulated by NoahMP-WRF is calculated using surface runoff only (Figure A7A) it performs better against observed DOQ_{25}; however, the projected sensitivity in streamflow timing to climate change remains significantly lower that predictions by the space-for-time substitution (Figure A7C). The fact that NoahMP-WRF has a biased DOQ_{25} simulation represents a challenge that goes beyond the scope of this study; however, these simulations have been tested in detail in terms of the meteorology and snow components (Liu et al., 2017; Scaff et al., 2020) and have been used for climate change analyses (Musselman et al., 2017, 2018). We used these simulations in the analysis because NoahMP underlies the US National Water Model and thus its

relevance to policy and research is high. There are many differences in the way that NoahMP-WRF and the space-for-time approach simulate the sensitivity of streamflow timing. NoahMP-WRF operating at sub-daily time steps has several advantages over space-for-time substitution. For example, NoahMP-WRF can track the hourly covariance in precipitation, temperature, and humidity to estimate precipitation partitioning between rain and snow. It is also able to represent hourly radiative and turbulent energy at the snowpack, and the cold content needed to predict snowmelt. The physical hydrology is also advanced and able to consider antecedent conditions and allow evapotranspiration losses that also modulate streamflow. Despite the advantages of land surface models like NoahMP-WRF in constraining processes for future projections, the simplicity of space-for-time substitution also provides several advantages. One of the main advantages is that it is derived from observations and thus it is well constrained by the observed spatial and temporal variability of snowmelt across watersheds and years (Figure 7B). Also, the space-for-time approach does not assume anything about the complex spatial distribution of snowpacks and precipitation or subsurface properties and interactions with the surface, which are major constraints to physically-based models (Baroni et al., 2010; Christiaens and Feyen, 2001; Wilby et al., 2002). While a space-for-time approach is not a replacement for land surface models like NoahMP-WRF, partly because the underlying streamflow datasets are not available everywhere, we believe that there is added value in including new benchmarks like the proposed DOS_{20} to further constrain modeling decisions and improve model fidelity required for reliable and accurate hydrological predictions.

5 Conclusions

Water management in the western US relies on accurate predictions of how both short-term climate variability and long-term climate change will alter snowmelt and streamflow. Differences in predictions of snowmelt-induced streamflow between empirical space-for-time projections and a land surface model (NoahMP-WRF) raise important questions about the sensitivity of streamflow timing to climate change, particularly in cold regions, and its impact on water planning. Significant differences exist in the way space-for-time substitution and land surface models predict changes to snowmelt and streamflow timing, with both approaches having strengths and weaknesses; however, the land surface model misrepresents historical patterns in streamflow response that at are more accurately estimated by the empirical space-for-time model. Specifically, we show that DOS_{20} is a strong predictor of the early season hydrograph response, particularly in cold, sunny areas where the NoahMP-WRF streamflow timing simulations lack sensitivity to climate change. Rigorously validating future model predictions is impossible, but snowmelt and streamflow timing, inferred from diel streamflow cycles, could be used to refine land surface models and better determine the risk to valuable snow water resources (Barnett et al., 2005; Sturm et al., 2017; Viviroli et al., 2007), particularly in cold regions. Our novel approach that can complement the benchmarking or calibration of physically based hydrological models, beyond typical benchmarking against daily streamflow or snow accumulation metrics. For example, the snowmelt timing metric DOS_{20}, based on diel streamflow observations, could be used to test the performance of land surface models running at sub-daily scales and fine spatial resolution in representing the historical snowmelt regime across watersheds and years. As land surface models move towards real application for water management (Kopp et al., 2018), the

hydrology community must seek ways to test and improve models using widely-available datasets if we are to meet the grand water management challenges posed by climate change and altered snowmelt regimes in key mountainous regions.

Acknowledgments

This project was supported by a grant with the Center for Weather and Water Extremes in the West (CW3E) and a National Science Foundation grant (EAR #2012310) to A.A. Harpold. S.A. Krogh thanks CONICYT for providing financial support through the Becas Chile program for postdoctoral studies. We appreciate the positive feedback and suggestions from Professor Jessica Lundquist and an anonymous reviewer, which greatly improved the discussion of the paper.

Contributions

SK and AH designed the study. SK performed the analysis, prepared the figures, and drafted the first version of the manuscript. JK developed the 'diel cycle index' which served as the initial idea for the presented snowmelt detection method. GS collected and pre-processed USGS hourly streamflow data and NLDAS-2 solar radiation. LS pre-processed daily surface and subsurface runoff from the WRF CONUS-I simulations. All the authors reviewed and contributed to the final version of the manuscript.

Competing Interests

The authors declare that they have no conflict of interest.

Code/Data availability

Data from NoahMP-WRF simulations can be access through their public website https://rda.ucar.edu/datasets/ds612.5/. Hourly shortwave radiation can be accessed online through: https://ldas.gsfc.nasa.gov/nldas/v2/forcing. Hourly streamflow from the USGS database can be accessed online through: https://waterdata.usgs.gov/nwis/sw. The code used to process and analyze the data presented in the study is available upon request to the corresponding author.

6 References

Addor, N., Newman, A. J., Mizukami, N. and Clark, M. P.: The CAMELS data set: catchment attributes and meteorology for large-sample studies, Earth Syst. Sci, 21, 5293–5313, doi:10.5194/hess-21-5293-2017, 2017.

Barnett, T. P., Adam, J. C. and Lettenmaier, D. P.: Potential impacts of a warming climate on water availability in snow-dominated regions, Nature, 438(7066), 303–309, doi:10.1038/nature04141, 2005.

Barnhart, T. B., Molotch, N. P., Livneh, B., Harpold, A. A., Knowles, J. F. and Schneider, D.: Snowmelt rate dictates streamflow, Geophys. Res. Lett., 43(15), 8006–8016, doi:10.1002/2016GL069690, 2016.

Baroni, G., Facchi, A., Gandolfi, C., Ortuani, B., Horeschi, D. and van Dam, J. C.: Uncertainty in the determination of soil hydraulic parameters and its influence on the performance of two hydrological models of different complexity, Hydrol. Earth Syst. Sci., 14(2), 251–270, doi:10.5194/hess-14-251-2010, 2010.

Berghuijs, W. R., Woods, R. a. and Hrachowitz, M.: A precipitation shift from snow towards rain leads to a decrease in streamflow, Nat. Clim. Chang., 4(7), 583–586, doi:10.1038/nclimate2246, 2014.

Blois, J. L., Williams, J. W., Fitzpatrick, M. C., Jackson, S. T. and Ferrier, S.: Space can substitute for time in predicting climate-change effects on biodiversity, Proc. Natl. Acad. Sci., 110(23), 9374–9379, doi:10.1073/pnas.1220228110, 2013.

Blöschl, G., Bierkens, M. F. P., Chambel, A., Cudennec, C., Destouni, G., Fiori, A., Kirchner, J. W., McDonnell, J. J., Savenije, H. H. G., Sivapalan, M., Stumpp, C., Toth, E., Volpi, E., Carr, G., Lupton, C., Salinas, J., Széles, B., Viglione, A., Aksoy, H., Allen, S. T., Amin, A., Andréassian, V., Arheimer, B., Aryal, S. K., Baker, V., Bardsley, E., Barendrecht, M. H., Bartosova, A., Batelaan, O., Berghuijs, W. R., Beven, K., Blume, T., Bogaard, T., Borges de Amorim, P., Böttcher, M. E., Boulet, G., Breinl, K., Brilly, M., Brocca, L., Buytaert, W., Castellarin, A., Castelletti, A., Chen, X., Chen, Y., Chen, Y., Chifflard, P., Claps, P., Clark, M. P., Collins, A. L., Croke, B., Dathe, A., David, P. C., de Barros, F. P. J., de Rooij, G., Di Baldassarre, G., Driscoll, J. M., Duethmann, D., Dwivedi, R., Eris, E., Farmer, W. H., Feiccabrino, J., Ferguson, G., Ferrari, E., Ferraris, S., Fersch, B., Finger, D., Foglia, L., Fowler, K., Gartsman, B., Gascoin, S., Gaume, E., Gelfan, A., Geris, J., Gharari, S., Gleeson, T., Glendell, M., Gonzalez Bevacqua, A., González-Dugo, M. P., Grimaldi, S., Gupta, A. B., Guse, B., Han, D., Hannah, D., Harpold, A., Haun, S., Heal, K., Helfricht, K., Herrnegger, M., Hipsey, M., Hlaváčiková, H., Hohmann, C., Holko, L., Hopkinson, C., Hrachowitz, M., Illangasekare, T. H., Inam, A., Innocente, C., Istanbulluoglu, E., Jarihani, B., et al.: Twenty-three unsolved problems in hydrology (UPH) – a community perspective, Hydrol. Sci. J., 64(10), 1141–1158, doi:10.1080/02626667.2019.1620507, 2019.

Bowling, D. R., Logan, B. A., Hufkens, K., Aubrecht, D. M., Richardson, A. D., Burns, S. P., Anderegg, W. R. L., Blanken, P. D. and Eiriksson, D. P.: Limitations to winter and spring photosynthesis of a Rocky Mountain subalpine forest, Agric. For. Meteorol., 252(February 2017), 241–255, doi:10.1016/j.agrformet.2018.01.025, 2018.

Brooks, P. D., Chorover, J., Fan, Y., Godsey, S. E., Maxwell, R. M., McNamara, J. P. and Tague, C.: Hydrological partitioning in the critical zone: Recent advances and opportunities for developing transferable understanding of water cycle dynamics, Water Resour. Res., 51(9), 6973–6987, doi:10.1002/2015WR017039, 2015.

Broxton, P. D., Harpold, A. A., Biederman, J. A., Troch, P. A., Molotch, N. P. and Brooks, P. D.: Quantifying the effects of vegetation structure on snow accumulation and ablation in mixed-conifer forests, Ecohydrology, 8(6), 1073–1094, doi:10.1002/eco.1565, 2015.

Christiaens, K. and Feyen, J.: Analysis of uncertainties associated with different methods to determine soil hydraulic properties and their propagation in the distributed hydrological MIKE SHE model, J. Hydrol., 246(1–4), 63–81, doi:10.1016/S0022-1694(01)00345-6, 2001.

Cline, D. W.: Snow surface energy exchanges and snowmelt at a continental, midlatitude Alpine site, Water Resour. Res., 33(4), 689–701, doi:10.1029/97WR00026, 1997.

Clow, D. W.: Changes in the timing of snowmelt and streamflow in Colorado: A response to recent warming, J. Clim., 23(9), 2293–2306, doi:10.1175/2009JCLI2951.1, 2010.

Cooper, A. E., Kirchner, J. W., Wolf, S., Lombardozzi, D. L., Sullivan, B. W., Tyler, S. W. and Harpold, A. A.: Snowmelt causes different limitations on transpiration in a Sierra Nevada conifer forest, Agric. For. Meteorol., 291(September 2019), 108089, doi:10.1016/j.agrformet.2020.108089, 2020.

Fan, Y., Clark, M., Lawrence, D. M., Swenson, S., Band, L. E., Brantley, S. L., Brooks, P. D., Dietrich, W. E., Flores, A., Grant, G., Kirchner, J. W., Mackay, D. S., McDonnell, J. J., Milly, P. C. D., Sullivan, P. L., Tague, C., Ajami, H., Chaney, N., Hartmann, A., Hazenberg, P., McNamara, J., Pelletier, J., Perket, J., Rouholahnejad-Freund, E., Wagener, T., Zeng, X., Beighley, E., Buzan, J., Huang, M., Livneh, B., Mohanty, B. P., Nijssen, B., Safeeq, M., Shen, C., Verseveld, W., Volk, J. and Yamazaki, D.: Hillslope Hydrology in Global Change Research and Earth System Modeling, Water Resour. Res., 55(2), 1737–1772, doi:10.1029/2018WR023903, 2019.

Foster, L., Bearup, L., Molotch, N., Brooks, P. and Maxwell, R.: Energy budget increases reduce mean streamflow more than snow–rain transitions: using integrated modeling to isolate climate change impacts on Rocky Mountain hydrology, Environ. Res. Lett., 11(4), 044015, doi:10.1088/1748-9326/11/4/044015, 2016.

Gochis, D. J., Barlage, M., Cabell, R., Casali, M., Dugger, A., FitzGerald, K., McAllister, M., McCreight, J., RafieeiNasab, A., Read, L., Sampson, K., Yates, D. and Zhang, Y.: The WRF-Hydro modeling system technical description, (Version 5.1.1). [online] Available from: https://ral.ucar.edu/sites/default/files/public/projects/wrf_hydro/technical-description-user-guide/wrf-hydro-v5.1.1-technical-description.pdf, 2020.

Godsey, S. E., Aas, W., Clair, T. A., de Wit, H. A., Fernandez, I. J., Kahl, J. S., Malcolm, I. A., Neal, C., Neal, M., Nelson, S. J., Norton, S. A., Palucis, M. C., Skjelkvåle, B. L., Soulsby, C., Tetzlaff, D. and Kirchner, J. W.: Generality of fractal 1/f scaling in catchment tracer time series, and its implications for catchment travel time distributions, Hydrol. Process., 24(12), 1660–1671, doi:10.1002/hyp.7677, 2010.

Goulden, M. L. and Bales, R. C.: Mountain runoff vulnerability to increased evapotranspiration with vegetation expansion, Proc. Natl. Acad. Sci., 111(39), 14071–14075, doi:10.1073/pnas.1319316111, 2014.

Harpold, A., Brooks, P., Rajagopal, S., Heidbuchel, I., Jardine, A. and Stielstra, C.: Changes in snowpack accumulation and ablation in the intermountain west, Water Resour. Res., 48(11), doi:10.1029/2012WR011949, 2012.

Harpold, A. A. and Brooks, P. D.: Humidity determines snowpack ablation under a warming climate, Proc. Natl. Acad. Sci., 115(6), 1215–1220, doi:10.1073/pnas.1716789115, 2018.

Harpold, A. A., Rajagopal, S., Crews, J. B., Winchell, T. and Schumer, R.: Relative Humidity Has Uneven Effects on Shifts From Snow to Rain Over the Western U.S., Geophys. Res. Lett., 44(19), 9742–9750, doi:10.1002/2017GL075046, 2017.

He, C., Chen, F., Barlage, M., Liu, C., Newman, A., Tang, W., Ikeda, K. and Rasmussen, R.: Can Convection-Permitting Modeling Provide Decent Precipitation for Offline High-Resolution Snowpack Simulations Over Mountains?, J. Geophys. Res. Atmos., 124(23), 12631–12654, doi:10.1029/2019JD030823, 2019.

Hidalgo, H. G., Das, T., Dettinger, M. D., Cayan, D. R., Pierce, D. W., Barnett, T. P., Bala, G., Mirin, A., Wood, A. W., Bonfils, C., Santer, B. D. and Nozawa, T.: Detection and Attribution of Streamflow Timing Changes to Climate Change in the Western United States, J. Clim., 22(13), 3838–3855, doi:10.1175/2009JCLI2470.1, 2009.

Houze, R. A.: Orographic effects on precipitating clouds, Rev. Geophys., 50(1), RG1001, doi:10.1029/2011RG000365, 2012.

Immerzeel, W. W., Lutz, A. F., Andrade, M., Bahl, A., Biemans, H., Bolch, T., Hyde, S., Brumby, S., Davies, B. J., Elmore, A. C., Emmer, A., Feng, M., Fernández, A., Haritashya, U., Kargel, J. S., Koppes, M., Kraaijenbrink, P. D. A., Kulkarni, A. V., Mayewski, P. A., Nepal, S., Pacheco, P., Painter, T. H., Pellicciotti, F., Rajaram, H., Rupper, S., Sinisalo, A., Shrestha, A. B., Viviroli, D., Wada, Y., Xiao, C., Yao, T. and Baillie, J. E. M.: Importance and vulnerability of the world's water towers, Nature, 577(7790), 364–369, doi:10.1038/s41586-019-1822-y, 2020.

Jasechko, S., Kirchner, J. W., Welker, J. M. and McDonnell, J. J.: Substantial proportion of global streamflow less than three months old, Nat. Geosci., 9(2), 126–129, doi:10.1038/ngeo2636, 2016.

Jennings, K. S., Winchell, T. S., Livneh, B. and Molotch, N. P.: Spatial variation of the rain–snow temperature threshold across the Northern Hemisphere, Nat. Commun., 9(1), 1148, doi:10.1038/s41467-018-03629-7, 2018.

Jepsen, S. M., Molotch, N. P., Williams, M. W., Rittger, K. E. and Sickman, J. O.: Interannual variability of snowmelt in the Sierra Nevada and Rocky Mountains, United States: Examples from two alpine watersheds, Water Resour. Res., 48(2), 1–15, doi:10.1029/2011WR011006, 2012.

Jepsen, S. M., Harmon, T. C., Ficklin, D. L., Molotch, N. P. and Guan, B.: Evapotranspiration sensitivity to air temperature across a snow-influenced watershed: Space-for-time substitution versus integrated watershed modeling, J. Hydrol., 556, 645–659, doi:10.1016/j.jhydrol.2017.11.042, 2018.

Kirchner, J. W.: A double paradox in catchment hydrology and geochemistry, Hydrol. Process., 17(4), 871–874, doi:10.1002/hyp.5108, 2003.

Kirchner, J. W.: Getting the right answers for the right reasons: Linking measurements, analyses, and models to advance the science of hydrology, Water Resour. Res., 42(3), 1–5, doi:10.1029/2005WR004362, 2006.

Kirchner, J. W., Godsey, S. E., Solomon, M., Osterhuber, R., McConnell, J. R. and Penna, D.: The pulse of a montane ecosystem: coupling between daily cycles in solar flux, snowmelt, transpiration, groundwater, and streamflow at Sagehen Creek and Independence Creek, Sierra Nevada, USA, Hydrol. Earth Syst. Sci., 24(11), 5095–5123, doi:10.5194/hess-24-5095-2020, 2020.

Klesse, S., DeRose, R. J., Babst, F., Black, B. A., Anderegg, L. D. L., Axelson, J., Ettinger, A., Griesbauer, H., Guiterman, C. H., Harley, G., Harvey, J. E., Lo, Y., Lynch, A. M., O'Connor, C., Restaino, C., Sauchyn, D., Shaw, J. D., Smith, D. J., Wood, L., Villanueva-Díaz, J. and Evans, M. E. K.: Continental-scale tree-ring-based projection of Douglas-fir growth: Testing the limits of space-for-time substitution, Glob. Chang. Biol., 26(9), 5146–5163, doi:10.1111/gcb.15170, 2020.

Klos, P. Z., Link, T. E. and Abatzoglou, J. T.: Extent of the rain-snow transition zone in the western U.S. under historic and projected climate, Geophys. Res. Lett., 41(13), 4560–4568, doi:10.1002/2014GL060500, 2014.

Kopp, S., Cline, D., Miniat, C., Lucero, C., Rothlisberger, J., Levinson, D., Evett, S., Brusberg, M., Lowenfish, M., Strobel, M., Tschirhart, W., Rindahl, B., Holder, S. and Ables, M.: Perspectives on the National Water Model, Water Resour. IMPACT, 20(1), 10–11, 2018.

Krogh, S. A., Broxton, P. D., Manley, P. N. and Harpold, A. A.: Using Process Based Snow Modeling and Lidar to Predict the Effects of Forest Thinning on the Northern Sierra Nevada Snowpack, Front. For. Glob. Chang., 3(March), doi:10.3389/ffgc.2020.00021, 2020.

Leroux, N. R. and Pomeroy, J. W.: Modelling capillary hysteresis effects on preferential flow through melting and cold layered snowpacks, Adv. Water Resour., 107, 250–264, doi:10.1016/j.advwatres.2017.06.024, 2017.

Liu, C., Ikeda, K., Rasmussen, R., Barlage, M., Newman, A. J. A. J. A. J. A. J., Prein, A. F. A. F., Chen, F., Chen, L., Clark, M., Dai, A., Dudhia, J., Eidhammer, T., Gochis, D., Gutmann, E., Kurkute, S., Li, Y., Thompson, G. and Yates, D.: Continental-scale convection-permitting modeling of the current and future climate of North America, Clim. Dyn., 49(1–2), 71–95, doi:10.1007/s00382-016-3327-9, 2017.

Loheide, S. P. and Lundquist, J. D.: Snowmelt-induced diel fluxes through the hyporheic zone, Water Resour. Res., 45(7), 1–9, doi:10.1029/2008WR007329, 2009.

Lundquist, J. D. and Cayan, D. R.: Seasonal and Spatial Patterns in Diurnal Cycles in Streamflow in the Western United States, J. Hydrometeorol., 3(5), 591–603, doi:10.1175/1525-7541(2002)003<0591:SASPID>2.0.CO;2, 2002.

Lundquist, J. D. and Dettinger, M. D.: How snowpack heterogeneity affects diurnal streamflow timing, Water Resour. Res., 41(5), 1–14, doi:10.1029/2004WR003649, 2005.

Lundquist, J. D., Cayan, D. R. and Dettinger, M. D.: Spring Onset in the Sierra Nevada: When Is Snowmelt Independent of Elevation?, J. Hydrometeorol., 5(2), 327–342, doi:10.1175/1525-7541(2004)005<0327:SOITSN>2.0.CO;2, 2004.

Lundquist, J. D., Dickerson-Lange, S. E., Lutz, J. A. and Cristea, N. C.: Lower forest density enhances snow retention in regions with warmer winters: A global framework developed from plot-scale observations and modeling, Water Resour. Res., 49(10), 6356–6370, doi:10.1002/wrcr.20504, 2013.

Luo, L., Robock, A., Mitchell, K. E., Houser, P. R., Wood, E. F., Schaake, J. C., Lohmann, D., Cosgrove, B., Wen, F., Sheffield, J., Duan, Q., Higgins, R. W., Pinker, R. T. and Tarpley, J. D.: Validation of the North American Land Data Assimilation System (NLDAS) retrospective forcing over the southern Great Plains, J. Geophys. Res. Atmos., 108(D22), 2002JD003246, doi:10.1029/2002JD003246, 2003.

Marks, D. and Dozier, J.: Climate and Energy Exchange at the Snow Surface in the Alpine Region of the Sierra Nevada 2 .

Snow Cover Energy Balance, Water Resour. Res., 28(11), 3043–3054, 1992.

Mazurkiewicz, A. B., Callery, D. G. and McDonnell, J. J.: Assessing the controls of the snow energy balance and water available for runoff in a rain-on-snow environment, J. Hydrol., 354(1–4), 1–14, doi:10.1016/j.jhydrol.2007.12.027, 2008.

McCabe, G. J. and Clark, M. P.: Trends and Variability in Snowmelt Runoff in the Western United States, J. Hydrometeorol., 6(4), 476–482, doi:10.1175/JHM428.1, 2005.

Meira Neto, A. A., Niu, G., Roy, T., Tyler, S. and Troch, P. A.: Interactions between snow cover and evaporation lead to higher sensitivity of streamflow to temperature, Commun. Earth Environ., 1(1), 56, doi:10.1038/s43247-020-00056-9, 2020.

Milly, P. C. D. and Dunne, K. A.: Colorado River flow dwindles as warming-driven loss of reflective snow energizes evaporation, Science (80-.)., 367(6483), 1252–1255, doi:10.1126/science.aay9187, 2020.

Mote, P. W., Li, S., Lettenmaier, D. P., Xiao, M. and Engel, R.: Dramatic declines in snowpack in the western US, npj Clim. Atmos. Sci., 1(1), 2, doi:10.1038/s41612-018-0012-1, 2018.

Müller, M. D. and Scherer, D.: A Grid- and Subgrid-Scale Radiation Parameterization of Topographic Effects for Mesoscale Weather Forecast Models, Mon. Weather Rev., 133(6), 1431–1442, doi:10.1175/MWR2927.1, 2005.

Musselman, K. N., Clark, M. P., Liu, C., Ikeda, K. and Rasmussen, R.: Slower snowmelt in a warmer world, Nat. Clim. Chang., 7(3), 214–219, doi:10.1038/nclimate3225, 2017.

Musselman, K. N., Lehner, F., Ikeda, K., Clark, M. P., Prein, A. F., Liu, C., Barlage, M. and Rasmussen, R.: Projected increases and shifts in rain-on-snow flood risk over western North America, Nat. Clim. Chang., 8(September), doi:10.1038/s41558-018-0236-4, 2018.

Mutzner, R., Weijs, S. V., Tarolli, P., Calaf, M., Oldroyd, H. J. and Parlange, M. B.: Controls on the diurnal streamflow cycles in two subbasins of an alpine headwater catchment, Water Resour. Res., 51(5), 3403–3418, doi:10.1002/2014WR016581, 2015.

Newman, A. J., Clark, M. P., Sampson, K., Wood, A., Hay, L. E., Bock, A., Viger, R. J., Blodgett, D., Brekke, L., Arnold, J. R., Hopson, T. and Duan, Q.: Development of a large-sample watershed-scale hydrometeorological data set for the contiguous USA: data set characteristics and assessment of regional variability in hydrologic model performance, Hydrol. Earth Syst. Sci., 19(1), 209–223, doi:10.5194/hess-19-209-2015, 2015.

Niu, G. Y., Yang, Z. L., Mitchell, K. E., Chen, F., Ek, M. B., Barlage, M., Kumar, A., Manning, K., Niyogi, D., Rosero, E., Tewari, M. and Xia, Y.: The community Noah land surface model with multiparameterization options (Noah - MP): 1 . Model description and evaluation with local - scale measurements, J. Geophys. Res., 116, 1–19, doi:10.1029/2010JD015139, 2011.

Ohmura, A.: Physical Basis for the Temperature-Based Melt-Index Method, J. Appl. Meteorol., 40(4), 753–761, doi:10.1175/1520-0450(2001)040<0753:PBFTTB>2.0.CO;2, 2001.

Pelletier, J. D., Broxton, P. D., Hazenberg, P., Zeng, X., Troch, P. A., Niu, G., Williams, Z., Brunke, M. A. and Gochis, D.: A gridded global data set of soil, intact regolith, and sedimentary deposit thicknesses for regional and global land surface modeling, J. Adv. Model. Earth Syst., 8(1), 41–65, doi:10.1002/2015MS000526, 2016.

Pomeroy, J. W., Parviainen, J., Hedstrom, N. and Gray, D. M.: Coupled modelling of forest snow interception and sublimation,

Hydrol. Process., 12(15), 2317–2337, doi:10.1002/(SICI)1099-1085(199812)12:15<2317::AID-HYP799>3.0.CO;2-X, 1998.

Regonda, S. K., Rajagopalan, B., Clark, M. and Pitlick, J.: Seasonal Cycle Shifts in Hydroclimatology over the Western United States, J. Clim., 18(2), 372–384, doi:10.1175/JCLI-3272.1, 2005.

Safa, H., Krogh, S. A., Greenberg, J., Kostadinov, T. S. and Harpold, A. A.: Unraveling the Controls on Snow Disappearance in Montane Conifer Forests Using Multi-Site Lidar, Water Resour. Res., 57(12), 1–20, doi:10.1029/2020WR027522, 2021.

Safeeq, M., Grant, G. E., Lewis, S. L. and Tague, C. L.: Coupling snowpack and groundwater dynamics to interpret historical streamflow trends in the western United States, Hydrol. Process., 27(5), 655–668, doi:10.1002/hyp.9628, 2013.

Scaff, L., Prein, A. F., Li, Y., Liu, C., Rasmussen, R. and Ikeda, K.: Simulating the convective precipitation diurnal cycle in North America's current and future climate, Clim. Dyn., 55(1–2), 369–382, doi:10.1007/s00382-019-04754-9, 2020.

Serreze, M. C., Clark, M. P., Armstrong, R. L., McGinnis, D. A. and Pulwarty, R. S.: Characteristics of the western United States snowpack from snowpack telemetry (SNOTEL) data, Water Resour. Res., 35(7), 2145–2160, doi:10.1029/1999WR900090, 1999.

Sivapalan, M., Yaeger, M. A., Harman, C. J., Xu, X. and Troch, P. A.: Functional model of water balance variability at the catchment scale: 1. Evidence of hydrologic similarity and space-time symmetry, Water Resour. Res., 47(2), 1–18, doi:10.1029/2010WR009568, 2011.

Skamarock, W. C., Klemp, J. B., Dudhi, J., Gill, D. O., Barker, D. M., Duda, M. G., Huang, X.-Y., Wang, W. and Powers, J. G.: A Description of the Advanced Research WRF Version 3, Boulder, Colorado, USA., 2008.

Stewart, I. T., Cayan, D. R. and Dettinger, M. D.: Changes in Snowmelt Runoff Timing in Western North America under a `Business as Usual' Climate Change Scenario, Clim. Change, 62(1–3), 217–232, doi:10.1023/B:CLIM.0000013702.22656.e8, 2004.

Stewart, I. T., Cayan, D. R. and Dettinger, M. D.: Changes toward Earlier Streamflow Timing across Western North America, J. Clim., 18(8), 1136–1155, doi:10.1175/JCLI3321.1, 2005.

Sturm, M., Goldstein, M. A. and Parr, C.: Water and life from snow: A trillion dollar science question, Water Resour. Res., 53(5), 3534–3544, doi:10.1002/2017WR020840, 2017.

Sumargo, E. and Cayan, D. R.: The Influence of Cloudiness on Hydrologic Fluctuations in the Mountains of the Western United States, Water Resour. Res., 54(10), 8478–8499, doi:10.1029/2018WR022687, 2018.

Tague, C. and Grant, G. E.: Groundwater dynamics mediate low-flow response to global warming in snow-dominated alpine regions, Water Resour. Res., 45(7), 1–12, doi:10.1029/2008WR007179, 2009.

Urióstegui, S. H., Bibby, R. K., Esser, B. K. and Clark, J. F.: Quantifying annual groundwater recharge and storage in the central Sierra Nevada using naturally occurring 35 S, Hydrol. Process., 31(6), 1382–1397, doi:10.1002/hyp.11112, 2017.

Viviroli, D., Dürr, H. H., Messerli, B., Meybeck, M. and Weingartner, R.: Mountains of the world, water towers for humanity: Typology, mapping, and global significance, Water Resour. Res., 43(7), 1–13, doi:10.1029/2006WR005653, 2007.

Viviroli, D., Archer, D. R., Buytaert, W., Fowler, H. J., Greenwood, G. B., Hamlet, A. F., Huang, Y., Koboltschnig, G., Litaor, M. I., López-Moreno, J. I., Lorentz, S., Schädler, B., Schreier, H., Schwaiger, K., Vuille, M. and Woods, R.: Climate change

and mountain water resources: overview and recommendations for research, management and policy, Hydrol. Earth Syst. Sci., 15(2), 471–504, doi:10.5194/hess-15-471-2011, 2011.

Wayand, N. E., Lundquist, J. D. and Clark, M. P.: Modeling the influence of hypsometry, vegetation, and storm energy on snowmelt contributions to basins during rain-on-snow floods, Water Resour. Res., 51(10), 8551–8569, doi:10.1002/2014WR016576, 2015.

Weiler, M., Seibert, J. and Stahl, K.: Magic components-why quantifying rain, snowmelt, and icemelt in river discharge is not easy, Hydrol. Process., 32(1), 160–166, doi:10.1002/hyp.11361, 2018.

Wilby, R. ., Dawson, C. . and Barrow, E. .: Sdsm — a Decision Support Tool for the Assessment of Regional Climate Change Impacts, Environ. Model. Softw., 17(2), 145–157, doi:10.1016/S1364-8152(01)00060-3, 2002.

Winchell, T. S., Barnard, D. M., Monson, R. K., Burns, S. P. and Molotch, N. P.: Earlier snowmelt reduces atmospheric carbon uptake in midlatitude subalpine forests, Geophys. Res. Lett., 43(15), 8160–8168, doi:10.1002/2016GL069769, 2016.

Woelber, B., Maneta, M. P., Harper, J., Jencso, K. G., Gardner, W. P., Wilcox, A. C. and López-Moreno, I.: The influence of diurnal snowmelt and transpiration on hillslope throughflow and stream response, Hydrol. Earth Syst. Sci., 22(8), 4295–4310, doi:10.5194/hess-22-4295-2018, 2018.

Wood, A. W. and Lettenmaier, D. P.: A Test Bed for New Seasonal Hydrologic Forecasting Approaches in the Western United States, Bull. Am. Meteorol. Soc., 87(12), 1699–1712, doi:10.1175/BAMS-87-12-1699, 2006.

Xia, Y., Mitchell, K., Ek, M., Sheffield, J., Cosgrove, B., Wood, E., Luo, L., Alonge, C., Wei, H., Meng, J., Livneh, B., Lettenmaier, D., Koren, V., Duan, Q., Mo, K., Fan, Y. and Mocko, D.: Continental-scale water and energy flux analysis and validation for the North American Land Data Assimilation System project phase 2 (NLDAS-2): 1. Intercomparison and application of model products, J. Geophys. Res. Atmos., 117(D3), 1–27, doi:10.1029/2011JD016048, 2012.

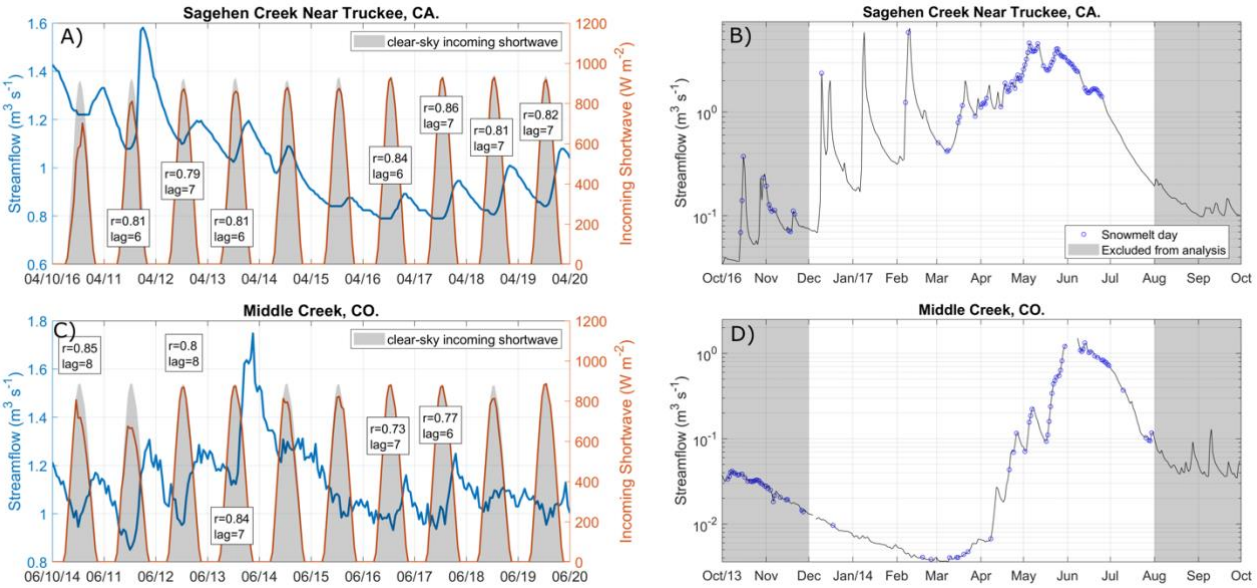

Figure 1: Examples of the diel cycle analysis applied to two watersheds located in California (A) (B) (WY2016) and Colorado (C) (D) (WY2014). (A) and (C) show hourly solar radiation (orange) and streamflow (blue); the first statistically significant ($p<0.01$) lagged spearman correlation ($r>0.6$) between streamflow and solar radiation is shown on a text box for clear-sky days only (>80% of clear-sky solar radiation). (B) and (D) show the solar radiation-driven snowmelt days (blue circles) on top of the annual hydrograph (semi-log scale) for the period of analysis (white background, December to July).

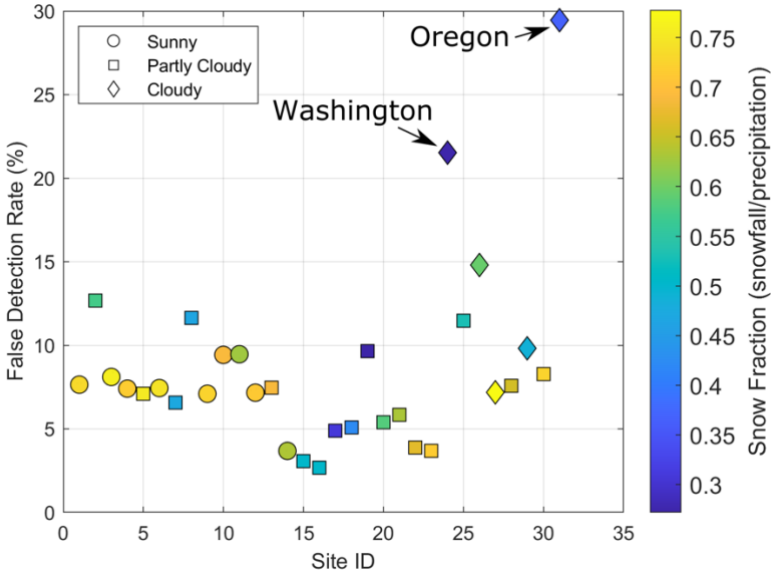

Figure 2: Percentage of days that were classified as having snowmelt following the diel streamflow cycle analysis that also had daily precipitation above 5 mm and a mean daily air temperature above 2 ºC. Symbols are associated with the mean annual percentage of snowmelt days under clear-sky conditions. Sunny sites (circles) have >90%, clear-sky snowmelt days, partly cloudy sites (squares) have between 70 and 90%, and cloudy sites (diamonds) have <70% clear-sky snowmelt days. Clear-sky snowmelt days are defined as those with more than 80% of the potential clear-sky solar radiation.

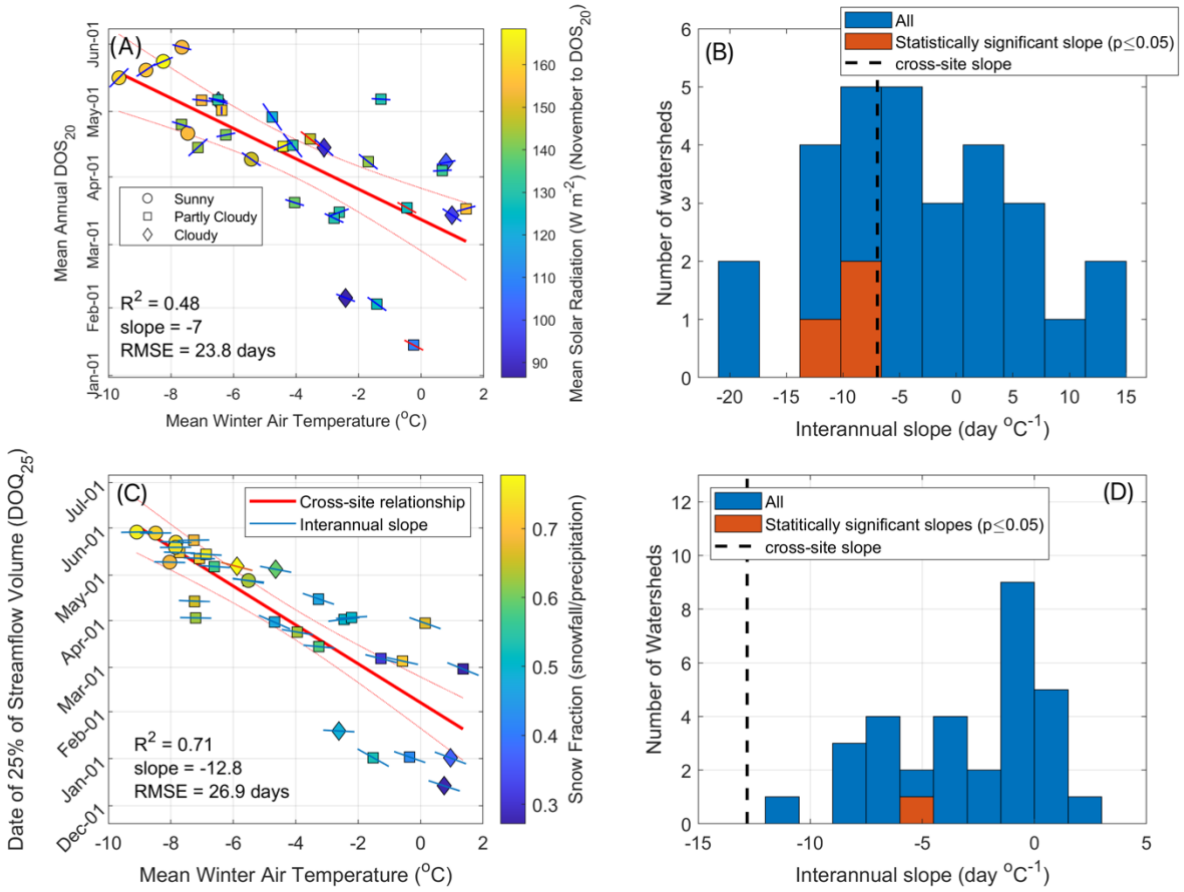

720 **Figure 3: (A) and (C) show cross-site relationships between mean winter air temperature (November to February) and DOS_{20} and the date of 25% of annual streamflow volume (DOQ_{25}), respectively. Slopes of individual sites' interannual relationships are shown as the lines on top of each symbol, where statistically significant (p-value ≤0.05) slopes are red. Non-significant interannual slopes are presented to show the overall tendency in their spatial distribution. Symbols are associated with the mean annual percentage of snowmelt days under clear-sky conditions. Sunny sites (circles) have >90% clear-sky snowmelt days, partly cloudy sites (squares)** 725 **have between 70 and 90%, and cloudy sites (diamonds) have <70% clear-sky snowmelt days. Clear-sky snowmelt days are defined as those with more than 80% of the potential clear-sky solar radiation. (B) and (D) show histograms of interannual slopes (for all watershed and those with statistically significant relationships) and the cross-site relationships presented in their respective left panel.**

730

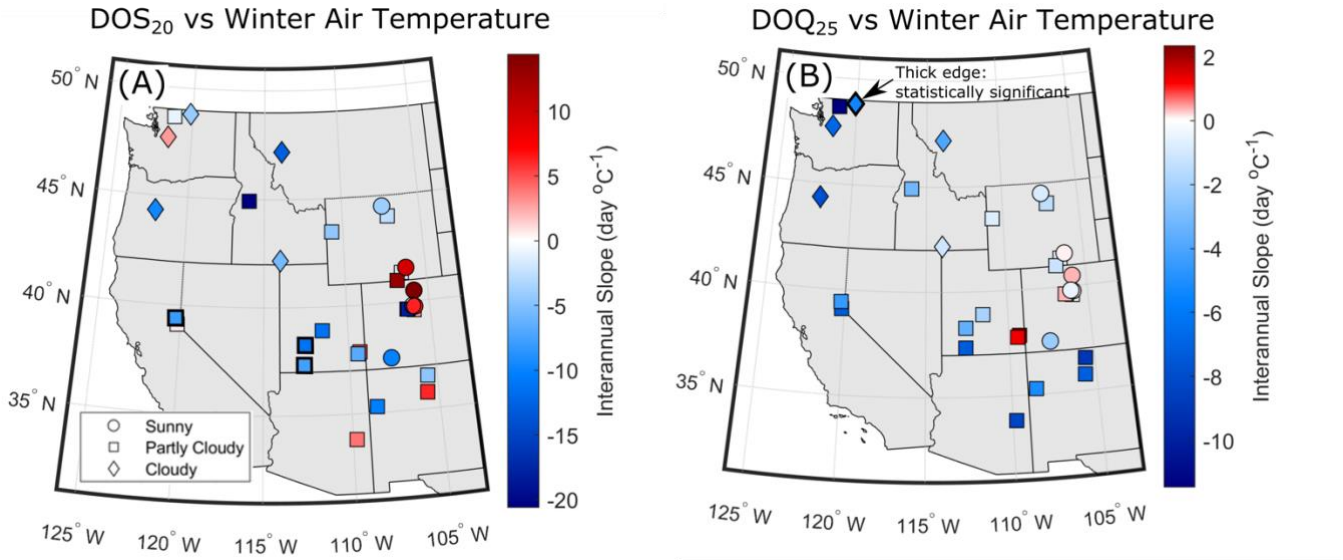

Figure 4: Spatial variability of watershed-level interannual slopes for (A) DOS_{20} vs winter air temperature, and (B) DOQ_{25} vs winter air temperature. Watersheds with statistically significant relationships are highlighted in symbols with thicker edges and are associated with those presented in Figure 3. Symbols are associated with the mean annual percentage of snowmelt days under clear-sky conditions. Sunny sites (circles) have >90% clear-sky snowmelt days, partly cloudy sites (squares) have between 70 and 90%, and cloudy sites (diamonds) have <70% clear-sky snowmelt days. Clear-sky snowmelt days are defined as those with more than 80% of the potential clear-sky solar radiation.

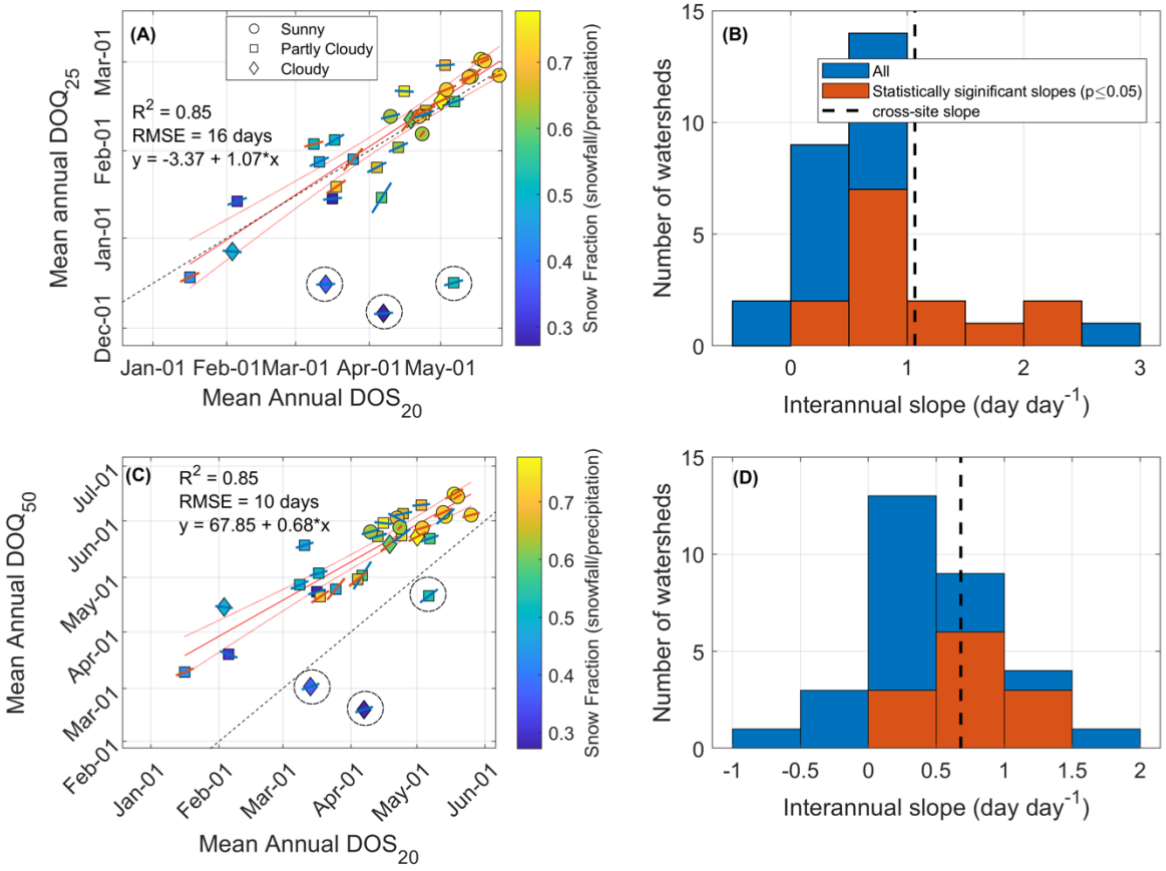

745 **Figure 5: (A) The day when the 20th percentile of snowmelt days occurs (DOS_{20}), compared to the date of the 25% of the annual streamflow volume (DOQ_{25}). (C) DOS_{20} against the date of 50% of the annual streamflow volume (DOQ_{50}). Dashed lines in (A) and (C) are 1:1 lines, and the slopes of sites' interannual relationships are shown as the lines on top of each symbol, with statistically significant (p-value ≤0.05) slopes shown in red. Sites #24, #25 and #31, indicated by dashed circles, fall far from the linear regression and are not included in its calculation. Symbols indicate the mean annual percentage of clear-sky snowmelt days, where sunny sites**
750 **(circles) have >90% clear-sky snowmelt days, partly cloudy sites (squares) have between 70 and 90%, and cloudy sites (diamonds) have <70%; clear-sky snowmelt days are defined as those with more than 80% of the potential clear-sky solar radiation. (B) and (D) show histograms of interannual slopes (for all watershed and those with statistically significant relationships) and the cross-site relationships presented in their respective left panels.**

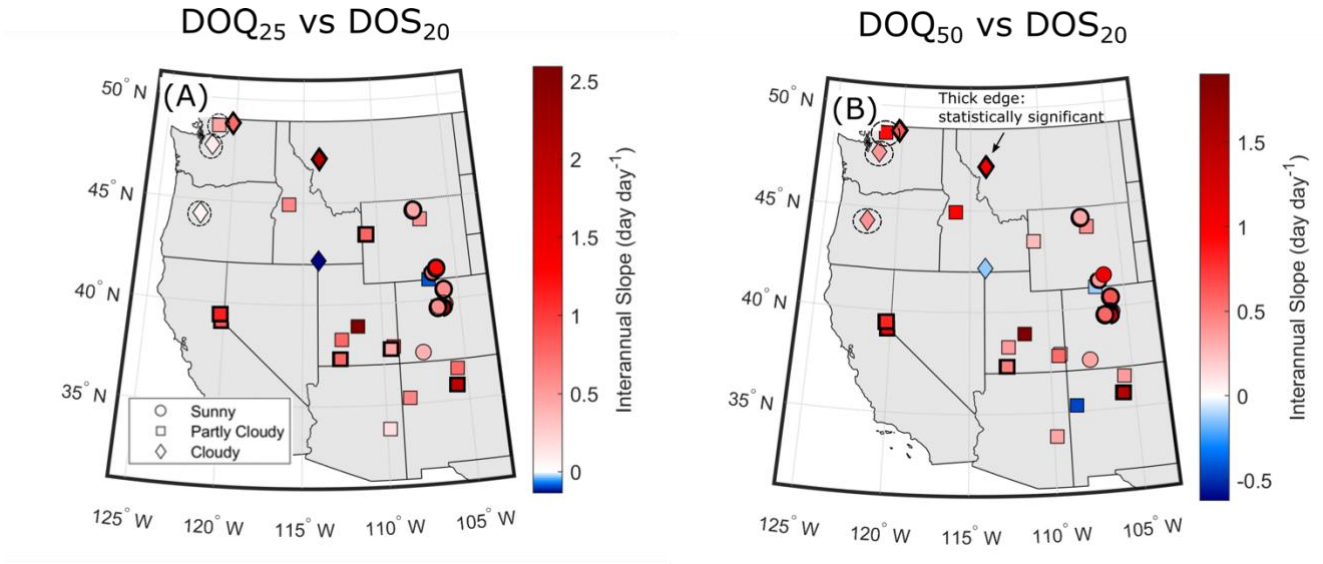

Figure 6: Spatial variability of the watershed-level interannual slopes for (A) DOQ_{25} vs DOS_{20}, and (B) DOQ_{50} vs DOS_{20}. Watersheds with statistically significant relationships are highlighted in symbols with thicker edges and are associated with those presented in Figure 5. Watersheds that fall far from the linear regression presented in Figure 5 are surrounded by a dashed circle. Symbols are associated with the mean annual percentage of snowmelt days under clear-sky conditions. Sunny sites (circles) have >90% clear-sky snowmelt days, partly cloudy sites (squares) have between 70 and 90%, and cloudy sites (diamonds) have <70%. Clear-sky snowmelt days are defined as those with more than 80% of the potential clear-sky solar radiation.

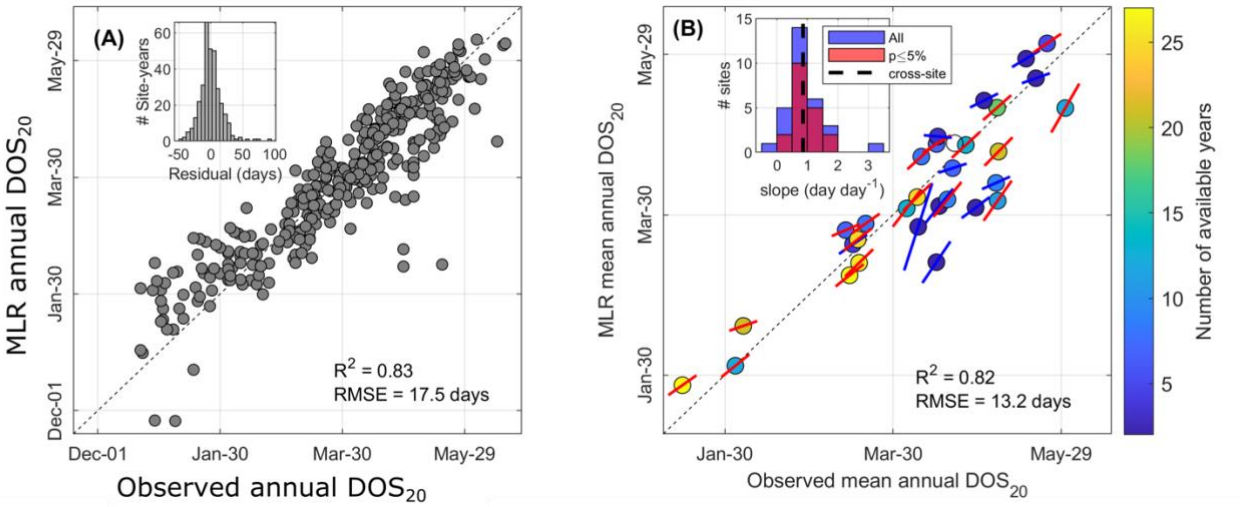

Figure 7: (A) scatterplot showing the fit of the stepwise multiple linear regression (MLR) model to the observed DOS_{20} across all sites and years. (B) shows the same stepwise MLR model applied at the mean annual watershed level across all watersheds. Interannual variability represented by the slope of the linear relationship is shown as a line overlapping each circle (i.e., watershed); red and blue lines indicate statistically significant ($p \leq 0.05$) and insignificant slopes, respectively.

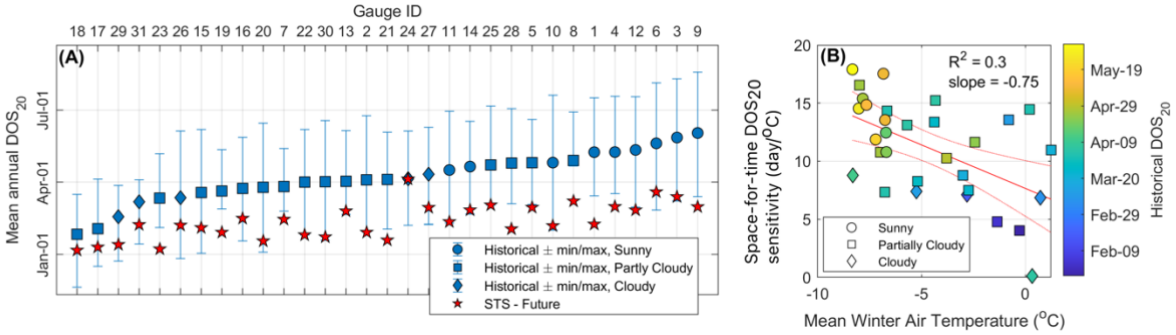

Figure 8: (A) Historical DOS_{20} from the diel analysis and projected changes in DOS_{20} using space-for-time projections under a RCP 8.5 pseudo global warming climate for the end of the 21st century. Watersheds are sorted from earlier (left) to later (right) historical DOS_{20}. Symbols associated with future projections (stars) are not classified by sunny, partly cloudy, or cloudy, as we make no inference about the cloudiness condition of snowmelt days under the climate change scenario. Blue symbols in (A) represent the mean annual percentage of clear-sky snowmelt days, where sunny sites (circles) have >90% clear-sky snowmelt days, partly cloudy sites (squares) have between 70 and 90%, and cloudy sites (diamonds) have <70%. Clear-sky snowmelt days are defined as those with more than 80% of the potential clear-sky solar radiation. (B) Relationship between mean winter air temperature and the sensitivity of DOS_{20} to climate change as projected by the space-for-time.

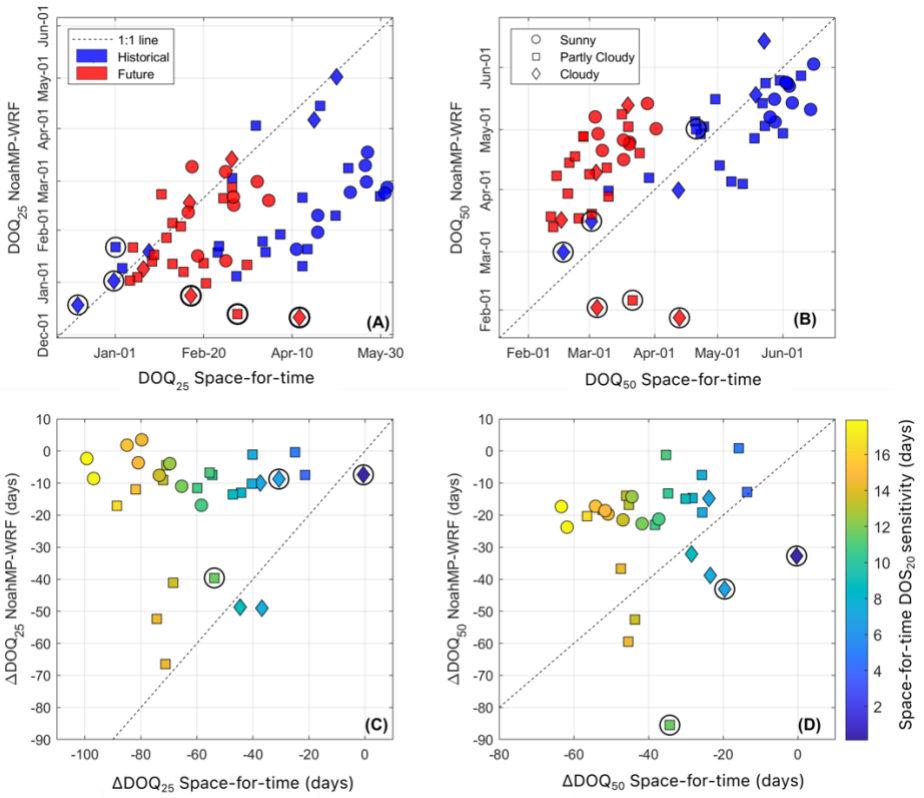

Figure 9: Changes to DOQ_{25} and DOQ_{50} due to climate change under an RCP8.5 pseudo global warming climate scenario by the end of the century. (A) and (B) compare historical against projected values between NoahMP-WRF and the space-for-time substitution. (C) and (D) compare the projected change (future minus historical) between NoahMP-WRF and space-for-time substitution, colored by the sensitivity of DOS_{20} to climate change as projected by the space-for-time analysis (Figure 8b). Symbols surrounded by black circles indicate sites that were excluded from the regression analysis in Figure 5 (rainier sites #24, #25 and #31). Symbols represent the historical mean annual percentage of clear-sky snowmelt days, where sunny sites (circles) have >90% clear-sky snowmelt days, partly cloudy sites (squares) have between 70 and 90%, and cloudy sites (diamonds) have <70%; clear-sky snowmelt days are defined as those with more than 80% of the potential clear-sky solar radiation. We make no inference about the cloudiness condition of snowmelt days under the RCP8.5 P climate scenario; however, red symbols (upper panels) follow the same symbology for easier interpretation.

800

Table 1: List of Abbreviations

Abbreviation	Definition
CAMELS	Catchments Attributes and MEteorology for Large-sample Studies
DOQ_{25}	Date of 25% of annual streamflow volume
DOQ_{50}	Date of 50% of annual streamflow volume
DOS_{20}	The day when the 20^{th} percentile of the snowmelt days occurs, with snowmelt days as defined by the streamflow diel cycle analysis
GCM	Global Climate Model
MLR	Multiple Linear Regression Model
NLDAS-2	Phase 2 of the National Land Data Assimilation System
Noah-MP	Noah Multi Parameterization land surface model
NoahMP-WRF	Simulations by WRF using the Noah-MP land surface model
RCP8.5	Representative Concentration Pathway 8.5
WRF	Weather Research and Forecasting Model

Table 2: List of the 31 watersheds from the CAMELS dataset included in this study. Data from Addor et al. (2017).

ID	USGS ID	Watershed Name	Drainage Area (km^2)	Mean Elevation (masl)	Mean slope (m km^{-1})	Lat. (°N)	Lon. (°W)	Snow Fraction	Aridity index	Soil Depth (m)
1	06278300	Shell Creek, WY.	58.9	2,953	86.7	44.51	107.40	0.73	1.32	0.74
2	06311000	North Fork Powder River, WY.	61.2	2,516	41.1	44.03	107.08	0.57	1.68	0.90
3	06614800	Michigan River, CO.	4.0	3,297	145.8	40.50	105.87	0.76	1.29	0.57
4	06622700	North Brush Creek, WY.	98.7	2,837	71.3	41.37	106.52	0.72	1.48	2.20
5	06623800	Encampment River, WY.	187.7	2,971	90.9	41.02	106.82	0.75	1.06	1.14
6	06632400	Rock Creek, WY.	163.0	3,002	69.0	41.59	106.22	0.74	1.46	2.52
7	08267500	Rio Hondo, NM.	96.3	3,007	149.1	36.54	105.56	0.47	2.12	0.50
8	08377900	Rio Mora, NM.	139.0	3,018	105.3	35.78	105.66	0.47	1.50	0.85
9	09034900	Bobtail Creek, CO.	15.7	3,571	102.8	39.76	105.91	0.73	1.16	0.47
10	09035900	South Fork of Williams Fork, CO.	72.8	3,241	123.9	39.80	106.03	0.69	1.44	0.56
11	09047700	Keystone Gulch, CO.	23.6	3,334	103.8	39.59	105.97	0.63	1.92	0.45
12	09066200	Booth Creek, CO.	16.1	3,072	145.4	39.65	106.32	0.71	1.40	0.27
13	09066300	Middle Creek, CO.	15.5	2,944	143.8	39.65	106.38	0.69	1.49	0.48
14	09352900	Vallecito Creek, CO.	188.2	3,283	156.1	37.48	107.54	0.63	1.24	0.50
15	09378170	South Creek, UT.	21.9	2,308	67.7	37.85	109.37	0.50	1.79	1.16
16	09378630	Recapture Creek, UT.	10.4	2,125	53.4	37.76	109.48	0.50	1.88	0.55
17	09386900	Rio Nutria, NM.	184.9	2,342	37.4	35.28	108.55	0.31	2.48	1.07
18	09404450	East Fork Virgin River, UT.	193.0	2,070	56.2	37.34	112.60	0.42	2.86	0.82
19	09492400	East Fork White River, AZ.	129.0	2,469	65.4	33.82	109.81	0.27	1.88	0.92
20	10205030	Salina Creek, UT.	134.6	2,489	76.2	38.91	111.53	0.58	2.46	0.67
21	10234500	Beaver River, UT.	236.4	2,499	95.2	38.28	112.57	0.63	2.06	0.60

22	10336660	Blackwood Creek, CA.	29.8	2,113	83.5	39.11	120.16	0.67	0.77	0.79
23	10343500	Sagehen Creek, CA.	27.6	2,157	81.2	39.43	120.24	0.71	1.10	1.20
24	12147600	South Fork Tolt River, WA.	14.1	1,068	159.4	47.71	121.60	0.27	0.22	0.63
25	12178100	Newhalem Creek, WA.	69.7	1,305	255.7	48.66	121.24	0.53	0.33	0.54
26	12381400	South Fork Jocko River, MT.	151.0	1,877	102.2	47.20	113.85	0.59	0.97	0.62
27	12447390	Andrews Creek, WA.	58.1	1,701	172.6	48.82	120.15	0.78	0.86	0.47
28	13018300	Cache Creek, WY.	27.9	2,198	109.5	43.45	110.70	0.66	1.50	0.69
29	13083000	Trapper Creek, ID.	133.2	1,863	69.1	42.17	113.98	0.49	2.11	1.04
30	13240000	Lake Fork Payette River, ID.	125.6	1,965	110.1	44.91	116.00	0.73	0.75	0.44
31	14158790	Smith River, OR.	40.6	1,027	116.4	44.33	122.05	0.37	0.36	0.85

805

7 Appendices

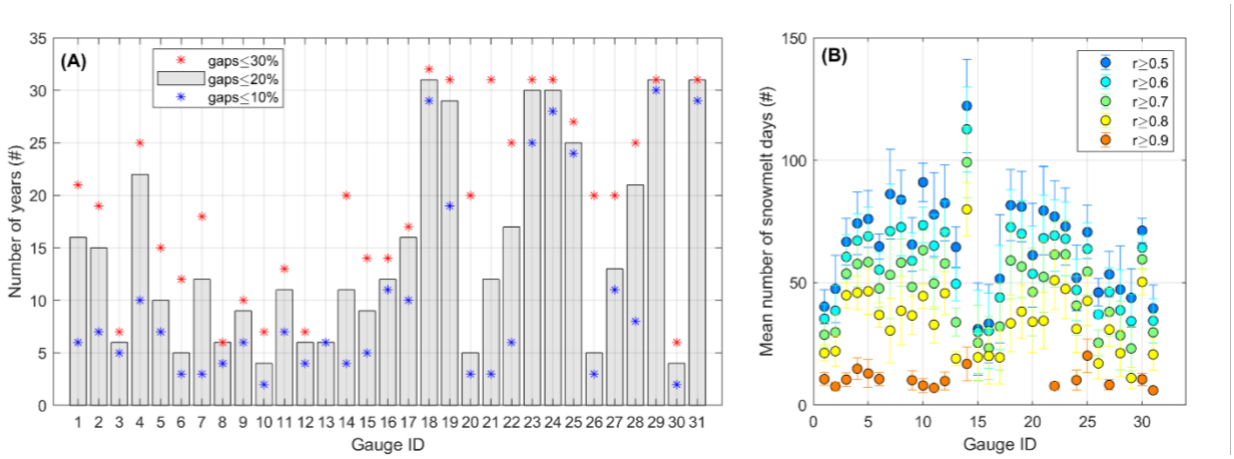

Figure A1: (A) Number of available years with less than 30, 20 and 10% gaps in days with hourly streamflow records between December 1 and August 1. Gauge ID is as presented in Table 2. Numbers of years at site #13 are the same for all thresholds (overlapping symbols). (B) Sensitivity of the mean annual number of detected snowmelt days to different Spearman correlation cutoffs (0.5, 0.6, 0.7 and 0.9) between hourly solar radiation and streamflow. Error bar represents the standard deviation.

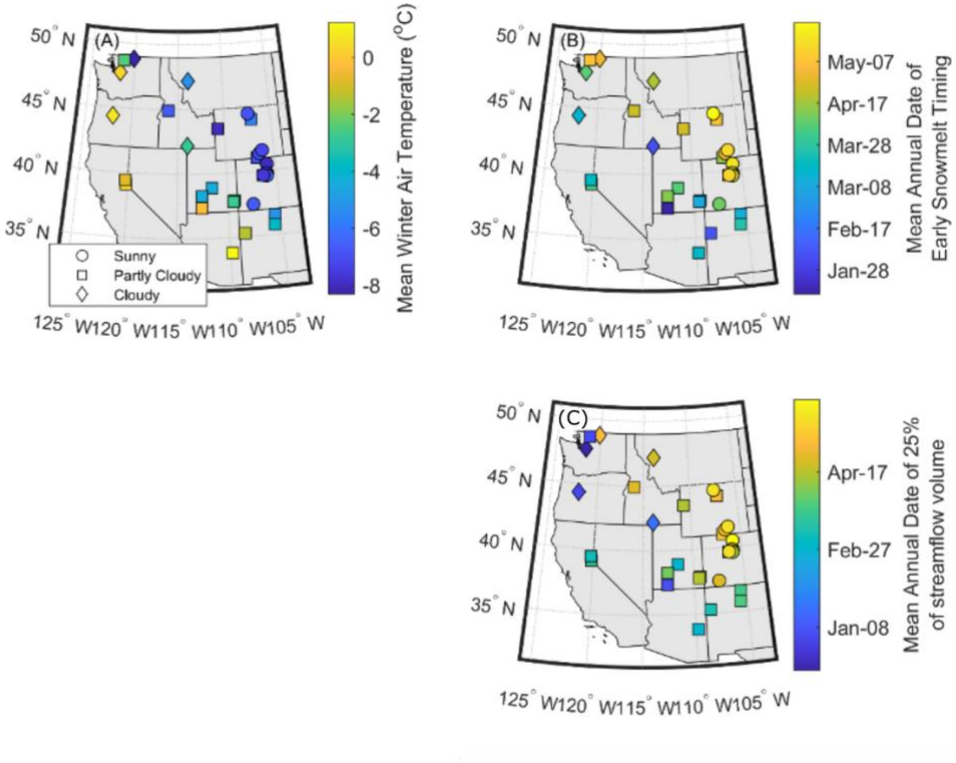

Figure A2: (A): CAMELS mean winter (November to February) air temperature, (B) mean annual DOS_{20}, and (C) mean annual DOQ_{25}. Symbols (circle, square and diamond) represent the mean annual percentage of clear-sky snowmelt days, where sunny sites have >90% clear-sky snowmelt days, partly cloudy have between 70 and 90%, and cloudy have <70%; clear-sky snowmelt days are defined as those with more than 80% of the potential clear-sky solar radiation.

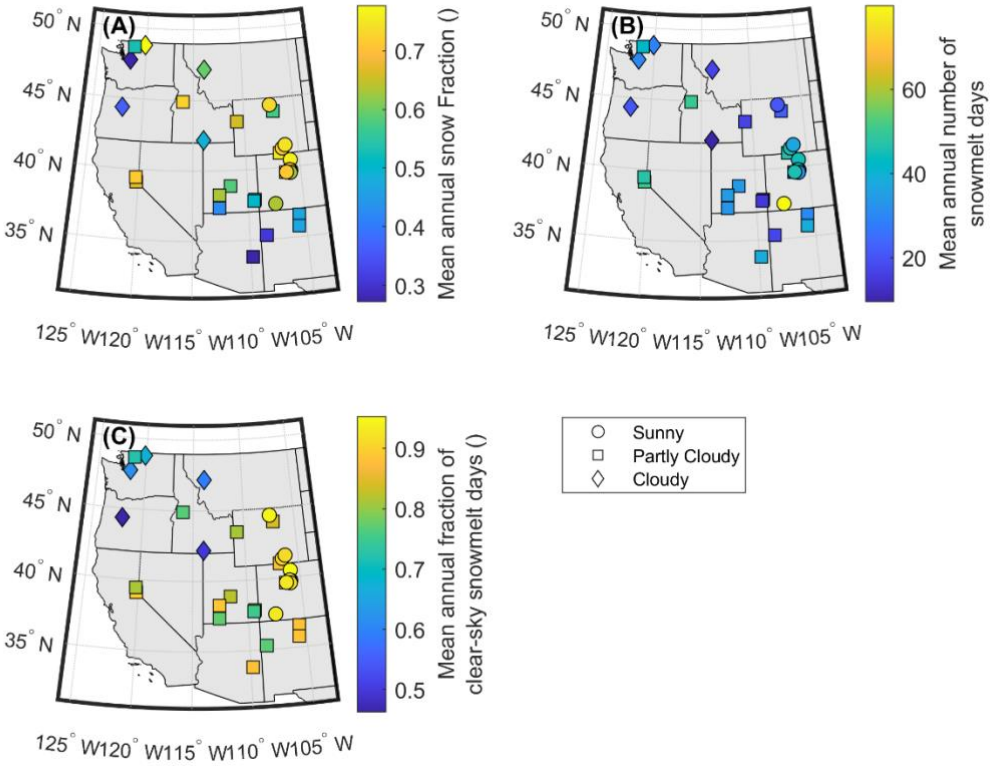

820

Figure A3: (A): CAMELS mean annual snow fraction (snowfall/precipitation), (B) mean annual number of snowmelt days between December 1 and August 1 (calculated as the days with a correlation between hourly solar radiation and lagged streamflow greater than 0.8), and (C) mean annual fraction of clear-sky snowmelt days, calculated as the number of snowmelt days with clear-sky conditions as a fraction of total snowmelt days. A clear-sky snowmelt day is defined as having more than 80% of the potential clear-
825 **sky solar radiation. Symbols (circle, square and diamond) represent the mean annual percentage of clear-sky snowmelt days, where sunny sites have >90% clear-sky snowmelt days, partly cloudy have between 70 and 90%, and cloudy have <70.**

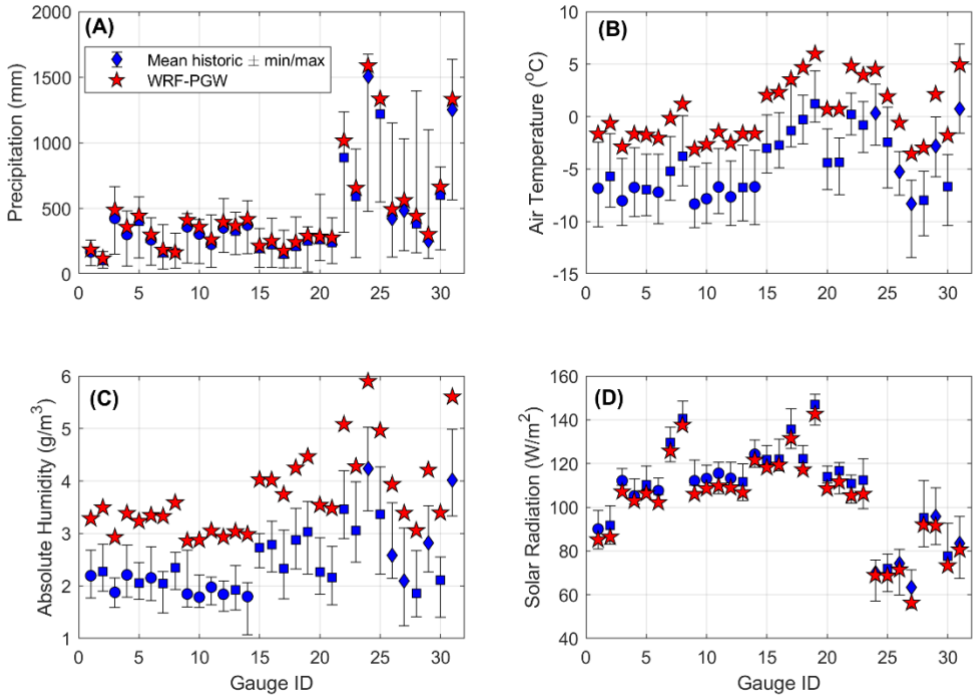

Figure A4: Historic winter climate variability for each predictor used in the stepwise MLR model (Equation 1) for the period between November and DOS_{20} in blue. (A) Precipitation, (B) air temperature, (C) absolute humidity and (D) solar radiation. In red are the perturbed mean climate variables under the RCP8.5 pseudo global warming scenario by the end of the century. This analysis suggests that most of the climate change signal from NoahMP-WRF pseudo global warming is within the observed climate variability, except for air temperature and atmospheric humidity in some watersheds. Blue symbols (circle, square and diamond) associated with historical values represent the mean annual percentage of clear-sky snowmelt days, where sunny sites have >90% clear-sky snowmelt days, partly cloudy have between 70 and 90%, and cloudy have <70%; clear-sky snowmelt days are defined as those with more than 80% of the potential clear-sky solar radiation. We make no inference about the cloudiness condition of snowmelt days under the RCP8.5 pseudo global warming scenario, and thus, we use a five-point star (in red) for the future scenario.

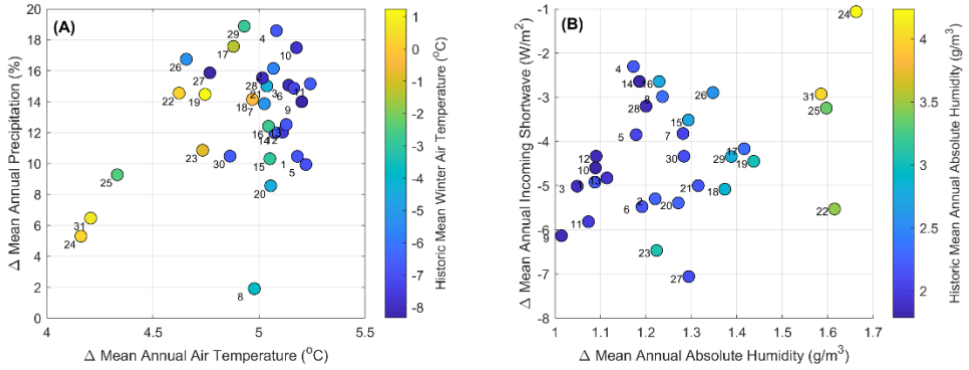

Figure A5: Mean annual climate changes projected by WRF under an RCP8.5 pseudo global warming scenario by the end of the century. (A) shows changes in precipitation against air temperature. (B) shows incoming shortwave against absolute humidity. Numbers represent the Gauge IDs as presented in Table 2.

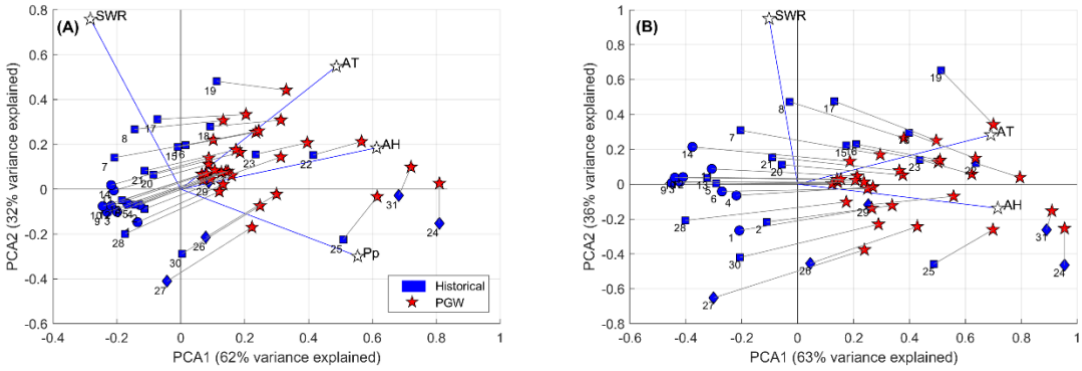

Figure A6: (A) Principal Component Analysis for historical precipitation (Pp), air temperature (AT), absolute humidity (AH) and shortwave radiation (SWR) at each watershed, and the changes associated with the pseudo global warming as simulated by WRF. (B) shows the same analysis but excluding precipitation from the analysis. Blue symbols (circle, square and diamond) associated with historical values represent the mean annual percentage of clear-sky snowmelt days, where sunny sites have >90% clear-sky snowmelt days, partly cloudy have between 70 and 90%, and cloudy have <70%; clear-sky snowmelt days are defined as those with more than 80% of the potential clear-sky solar radiation. We make no inference about the cloudiness condition during snowmelt days under the RCP8.5 pseudo global warming scenario, and thus, we use a five-point star (in red) for the future scenario. Numbers next to blue symbols represent the Gauge IDs as presented in Table 2.

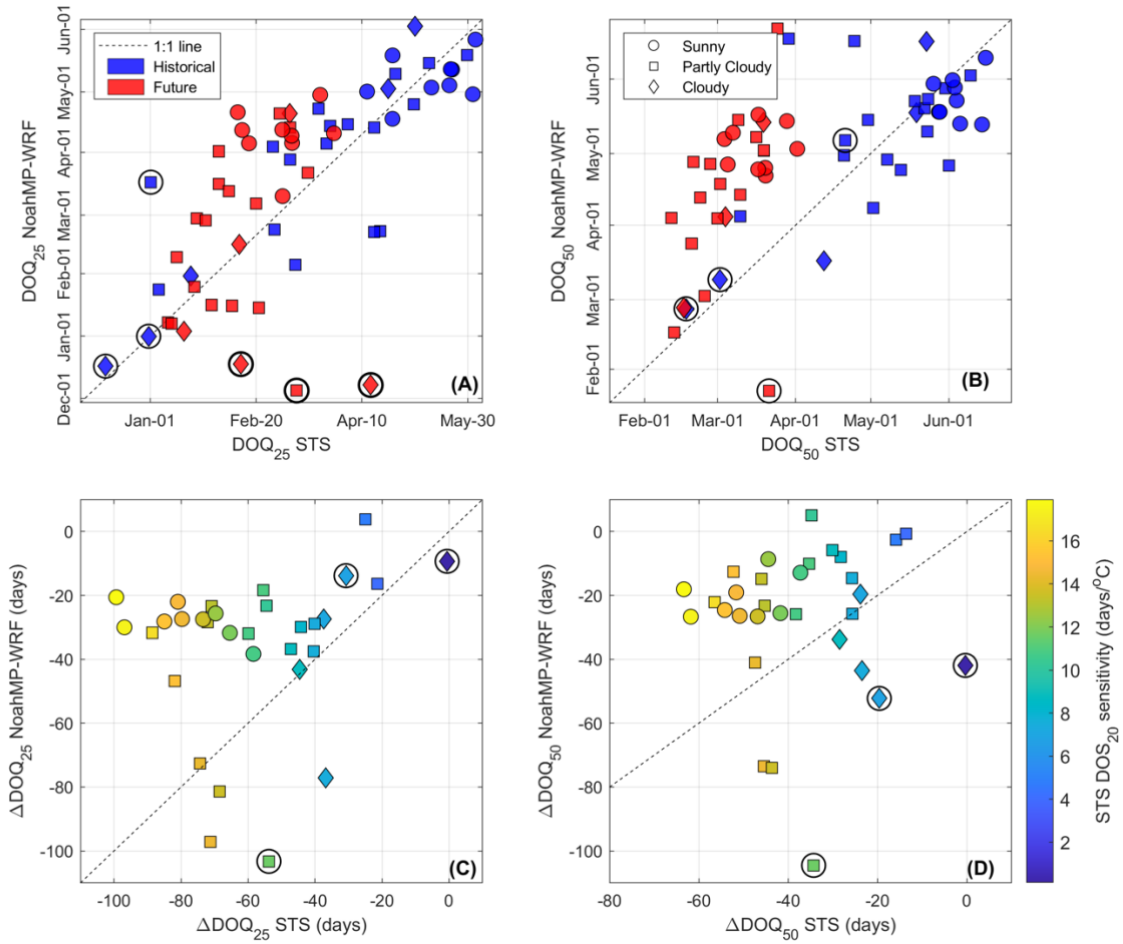

Figure A7: Same as Figure 9 but using streamflow timing metrics from NoahMP-WRF for an RCP8.5 pseudo global warming scenario, calculated using surface runoff only instead of using surface plus subsurface runoff (as in Figure 6). Note the improved fit in historical DOQ_{25}; however, this analysis yields very similar results to those of Figure 6, with NoahMP-WRF streamflow simulations being much less sensitive to climate change than space-for-time substitution would suggest. (A) and (B) compare historical against projected values between NoahMP-WRF and the space-for-time approach. (C) and (D) compare the projected change (future minus historical) between NoahMP-WRF and space-for-time, colored by the sensitivity of DOS_{20} to climate change as projected by the space-for-time analysis (Figure 5b). Symbols surrounded by black circles indicate sites that were excluded from the regression analysis in Figure 3 (rainier sites #24, #25 and #31). Symbols (circle, square and diamond) represent the historical mean annual percentage of clear-sky snowmelt days, where sunny sites have >90% clear-sky snowmelt days, partly cloudy have between 70 and 90%, and cloudy have <70%; clear-sky snowmelt days are defined as those with more than 80% of the potential clear-sky solar radiation. We make no inference about the cloudiness condition of snowmelt days under the RCP8.5 pseudo global warming climate scenario; however, red symbols (upper panels) follow the same symbology for easier interpretation.

Table A1: Coefficient of determination (R^2) and slope (in parenthesis, day/day) of the linear regression between different early snowmelt timing metrics and DOQ_{25} and DOQ_{50}, as presented in Figure 5, for different correlation cutoffs (r) between hourly solar radiation and streamflow. DOSxx represent the date when the xxth percentile of snowmelt days occurs. Sites #24, #35 and #31, are excluded from the linear relationship. Bolded numbers are those used in the result and discussion sections.

Early snowmelt timing metrics		vs DOQ_{25}	vs DOQ_{50}
r > 0.5	1st snowmelt day	0.13 (0.61)	0.06 (0.25)
	1st 3 consecutive snowmelt day	0.5 (0.71)	0.4 (0.4)
	DOS_5	0.37 (0.83)	0.28 (0.45)
	DOS_{10}	0.49 (0.91)	0.43 (0.52)
	DOS_{20}	0.69 (1.1)	0.66 (0.67)
	DOS_{30}	0.73 (1.1)	0.72 (0.68)
r > 0.6	1st snowmelt day	0.24 (0.73)	0.15 (0.35)
	1st 3 consecutive snowmelt day	0.59 (0.77)	0.49 (0.44)
	DOS_5	0.46 (0.82)	0.37 (0.45)
	DOS_{10}	0.63 (0.97)	0.53 (0.55)
	DOS_{20}	0.76 (1.05)	0.72 (0.64)
	DOS_{30}	0.77 (1.07)	0.78 (0.67)
r > 0.7	1st snowmelt day	0.42 (0.73)	0.3 (0.39)
	1st 3 consecutive snowmelt day	0.62 (0.85)	0.59 (0.53)
	DOS_5	0.61 (0.86)	0.51 (0.49)
	DOS_{10}	0.71 (0.94)	0.63 (0.55)
	DOS_{20}	0.76 (0.99)	0.75 (0.62)
	DOS_{30}	0.79 (1.03)	0.82 (0.65)
r > 0.8	1st snowmelt day	0.66 (0.87)	0.54 (0.5)
	1st 3 consecutive snowmelt day	0.76 (1.09)	0.78 (0.71)
	DOS_5	0.79 (1.01)	0.7 (0.6)
	DOS_{10}	0.83 (1.03)	0.78 (0.64)
	DOS_{20}	**0.85 (1.07)**	**0.85 (0.68)**
	DOS_{30}	0.85 (1.1)	0.88 (0.72)

Table A2: Root mean square error (RMSE) and coefficient of determination (R^2, in parentheses) associated with several stepwise multiple linear regressions (similar to the one in Equation 1) using different early snowmelt timing metrics (e.g., Equation 1 uses DOS_{20}) and correlation cutoffs (r) between hourly solar radiation and streamflow used to define snowmelt days. DOSxx represents the date when the xxth percentile of snowmelt days occurs. Bolded numbers are associated with the stepwise MLR in Equation 1 also shown in Figure 7A.

Early snowmelt timing metrics	**r > 0.5**	**r > 0.6**	**r > 0.7**	**r > 0.8**
First snowmelt day	11.1 (0.87)	12.3 (0.88)	15.2 (0.88)	21.7 (0.82)
First 3 consecutive snowmelt days	24.6 (0.8)	24.8 (0.8)	26.1 (0.77)	20.2 (0.8)
DOS_5	14.9 (0.83)	15.4 (0.85)	17.3 (0.86)	21.1 (0.8)
DOS_{10}	16.4 (0.82)	17.3 (0.83)	19.9 (0.82)	19.6 (0.82)
DOS_{20}	16.5 (0.82)	17.9 (0.82)	18.9 (0.82)	**17.5 (0.83)**
DOS_{30}	16.3 (0.82)	17.4 (0.82)	17.8 (0.82)	16.3 (0.83)

Table A3: Coefficient of determination (R^2) for the site-average stepwise multiple linear regression, analogous to that presented in Figure 7B, for different modeling decisions (correlation cutoff between hourly solar radiation and streamflow, r, and early snowmelt days metrics). DOSxx represents the date when the xxth percentile of snowmelt days occurs. Bolded number is associated with the stepwise MLR in Equation 1 using DOS_{20}.

Early snowmelt timing metrics	**r > 0.5**	**r > 0.6**	**r > 0.7**	**r > 0.8**
First snowmelt day	0.8	0.82	0.89	0.79
First 3 consecutive snowmelt days	0.81	0.77	0.73	0.69
DOS_5	0.84	0.85	0.87	0.83
DOS_{10}	0.84	0.85	0.86	0.84
DOS_{20}	0.83	0.82	0.82	**0.82**
DOS_{30}	0.83	0.81	0.81	0.8

Table A4: Standardized beta coefficients for the stepwise MLR associated with the different correlation cutoffs (r) between hourly solar radiation and streamflow, and different early snowmelt metrics. These stepwise MLR models follow the same structure as that of Equation 1; however, in this case predictors were standardized to estimate their relative importance. AT: Air Temperature, Pp: Precipitation, RH: Relative Humidity, SWR: Incoming Shortwave Radiation. DOSxx represent the date when the xxth percentile of snowmelt days occurs. *Indicates rows that do not meet all the MLR assumptions. Bolded numbers are associated with the modeling decisions used in the result and discussion sections.

Early snowmelt timing metrics		**β_1: AT**	**β_2: Pp**	**β_3: RH**	**β_4: SWR**	**β_5: ATxPp**	**β_6: ATxRH**	**β_7: ATxSWR**	**β_8: PpxRH**	**β_9: PpxSWR**	**β_{10}: RHxSWR**
r > 0.5	1st snowmelt day*	n/a	n/a	n/a	n/a	n/a	n/a	n/a	n/a	n/a	n/a
	1st 3 consecutive snowmelt days	-0.41	0.74	0.002	0.38	0.19	n/a	n/a	-0.33	n/a	-0.19
	DOS_5*	n/a	n/a	n/a	n/a	n/a	n/a	n/a	n/a	n/a	n/a
	DOS_{10}	-0.55	0.45	0.22	0.56	0.26	n/a	n/a	n/a	0.23	-0.21
	DOS_{20}	-0.39	0.46	0.33	0.68	0.10	n/a	n/a	-0.10	0.12	-0.28
	DOS_{30}	-0.32	0.39	0.38	0.76	n/a	0.06	n/a	n/a	0.15	-0.27
r > 0.6	1st snowmelt day*	n/a	n/a	n/a	n/a	n/a	n/a	n/a	n/a	n/a	n/a
	1st 3 consecutive snowmelt days	-0.39	0.69	0.03	0.43	0.15	n/a	n/a	-0.26	0.08	-0.21
	DOS_5*	n/a	n/a	n/a	n/a	n/a	n/a	n/a	n/a	n/a	n/a
	DOS_{10}	0.54	0.42	0.18	0.52	0.23	n/a	n/a	n/a	0.22	-0.16
	DOS_{20}	-0.35	0.41	0.31	0.69	0.10	n/a	n/a	-0.08	0.10	-0.24
	DOS_{30}	-0.30	0.33	0.37	0.75	0.07	n/a	n/a	n/a	0.15	-0.24
r > 0.7	1st snowmelt day*	n/a	n/a	n/a	n/a	n/a	n/a	n/a	n/a	n/a	n/a
	1st 3 consecutive snowmelt days	-0.45	0.69	0.03	0.46	n/a	0.11	n/a	-0.16	0.09	-0.23
	DOS_5*	n/a	n/a	n/a	n/a	n/a	n/a	n/a	n/a	n/a	n/a
	DOS_{10}	-0.46	0.39	0.20	0.55	0.21	-0.08	n/a	-0.09	0.11	-0.17
	DOS_{20}	-0.31	0.30	0.36	0.77	0.10	n/a	n/a	n/a	0.14	-0.24
	DOS_{30}	-0.29	0.29	0.38	0.77	0.08	n/a	n/a	n/a	0.17	-0.26
r > 0.8	1st snowmelt day	-0.57	0.41	0.08	0.34	0.28	n/a	n/a	n/a	0.21	-0.06
	1st 3 consecutive snowmelt days	-0.35	0.43	0.26	0.67	n/a	0.09	n/a	n/a	0.22	-0.27
	DOS_5	-0.43	0.39	0.21	0.56	0.23	n/a	n/a	-0.09	0.14	-0.19
	DOS_{10}	-0.34	0.37	0.28	0.68	0.16	n/a	n/a	-0.09	0.13	-0.26
	DOS_{20}	**-0.31**	**0.29**	**0.37**	**0.75**	**0.11**	**n/a**	**n/a**	**n/a**	**0.18**	**-0.29**
	DOS_{30}	-0.29	0.29	0.37	0.76	0.09	n/a	n/a	n/a	0.18	-0.26

Table A5: Coefficient of determination (R^2) and slope (in parenthesis, days $°C^{-1}$) of the linear regression between space-for-time sensitivity to warming and sites' mean winter air temperature as presented in Figure 8B, for different early snowmelt day metrics and correlation cutoffs (r) between hourly solar radiation and streamflow. DOSxx represent the date when the xx^{th} percentile of snowmelt days occurs. Bolded numbers are associated with the modeling decisions used in the result and discussion sections.

Early snowmelt timing metrics	**r > 0.5**	**r > 0.6**	**r > 0.7**	**r > 0.8**
First snowmelt day	0.08 (0.61)	0.09 (0.47)	0.03 (0.47)	0.23 (-0.75)
First 3 consecutive snowmelt days	0.02 (-0.30)	0.08 (-0.51)	0.00 (-0.05)	0.00 (-0.07)
DOS_5	0.00 (0.04)	0.01 (-0.18)	0.02 (-0.32)	0.25 (-1.00)
DOS_{10}	0.00 (-0.09)	0.25 (-0.86)	0.37 (-1.17)	0.2 (-0.66)
DOS_{20}	0.27 (-0.68)	0.35 (-0.89)	0.37 (-0.99)	**0.33 (-0.75)**
DOS_{30}	0.22 (-0.57)	0.26 (-0.65)	0.27 (-0.66)	0.20 (-0.52)